



AMERICAN METEOROLOGICAL SOCIETY

Journal of Applied Meteorology and Climatology

EARLY ONLINE RELEASE

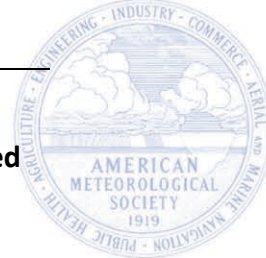
This is a preliminary PDF of the author-produced manuscript that has been peer-reviewed and accepted for publication. Since it is being posted so soon after acceptance, it has not yet been copyedited, formatted, or processed by AMS Publications. This preliminary version of the manuscript may be downloaded, distributed, and cited, but please be aware that there will be visual differences and possibly some content differences between this version and the final published version.

The DOI for this manuscript is doi: 10.1175/JAMC-D-18-0008.1

The final published version of this manuscript will replace the preliminary version at the above DOI once it is available.

If you would like to cite this EOR in a separate work, please use the following full citation:

Li, D., B. Yin, J. Feng, A. Dosio, B. Geyer, J. Qi, H. Shi, and Z. Xu, 2018: Present climate evaluation and added value analysis of dynamically downscaled simulations of CORDEX-East Asia. *J. Appl. Meteor. Climatol.* doi:10.1175/JAMC-D-18-0008.1, in press.



1 Present climate evaluation and added value analysis of dynamically downscaled 2 simulations of CORDEX-East Asia

3 Delei Li^{1,2,3}, Baoshu Yin^{1,2,3,8}, Jianlong Feng⁴, Alessandro Dosio⁵, Beate Geyer⁶, JiFeng
4 Qi^{1,2,3}, Hongyuan Shi⁷, Zhenhua Xu^{1,2,3*}

⁵Key Laboratory of Ocean Circulation and Waves, Institute of Oceanology, Chinese
⁶Academy of Sciences, Qingdao, China

⁷ ²Function Laboratory for Ocean Dynamics and Climate, Qingdao National Laboratory
for Marine Science and Technology, Qingdao, China

⁹ ³Center for Ocean Mega-Science, Chinese Academy of Sciences, Qingdao, China

¹⁰ ⁴National Marine Data and Information Service, Tianjin, China

¹¹ European Commission, Joint Research Centre, Ispra, Italy

12 ⁶Helmholtz-Zentrum Geesthacht Centre for Materials and Coastal Research,
13 Geesthacht, Germany

¹⁴ ⁷School of Civil Engineering, Ludong University, Yantai, China

¹⁵⁸University of Chinese Academy of Sciences, Beijing, China

16 Corresponding author: Zhenhua Xu, Email: xuzhenhua@qdio.ac.cn; Phone: 86-
17 053282888991

18 **Abstract**

19 In this study, we investigate the skills of the regional climate model COnsortium
20 for Small-scale MOdeling in CLimate Mode (CCLM) in reproducing historical climatic
21 features and their added value to the driving global climate models (GCMs) of the
22 Coordinated Regional Climate Downscaling Experiment – East Asia (CORDEX-EA)
23 domain. An ensemble of climate simulations, with resolution of 0.44° , was conducted
24 by downscaling four GCMs: CNRM-CM5, EC-EARTH, HadGEM2, and MPI-ESM-LR. The
25 CCLM outputs were compared against different observations and reanalysis datasets.

26 Results showed strong seasonal variability of CCLM's ability in reproducing
27 climatological means, variability and extremes. The bias of the simulated summer
28 temperatures is generally smaller than that of the winter temperatures; additionally,
29 areas where CCLM adds value to the driving GCMs in simulating temperature are larger
30 in the winter than in the summer. The CCLM outperforms GCMs in terms of generating
31 climatological precipitation means and daily precipitation distributions for most
32 regions in the winter; however, this is not always the case for the summer. It was found
33 that CCLM biases are partly inherited from GCMs and are significantly shaped by
34 structural biases of the CCLM. Furthermore, downscaled simulations show an added
35 value in capturing features of consecutive wet days for the tropics and of consecutive
36 dry days for northern areas to 30°N .

37 We found considerable uncertainty from reanalysis and observation datasets in
38 temperatures and precipitation climatological means for some regions that rival bias
39 values of GCMs and CCLM simulations. We recommend carefully selecting reference

40 datasets when evaluating modeled climate means.

41 **1. Introduction**

42 Climatic changes have significant impacts on natural and human systems
43 worldwide. In particular, changes in climate extremes such as heat waves, droughts
44 and floods associated with medium and high emissions scenarios for this century
45 present high risks of abrupt and irreversible changes to terrestrial and ocean
46 ecosystems, freshwater resources, food production and human health (IPCC 2014).

47 Global climate models (GCM) and earth system models (ESM) are the primary and
48 most comprehensive tools used to simulate past and future climatic change. They have
49 been demonstrated to capture climate variability and features at both continental and
50 global scales (Sperber et al. 2013). However, GCMs and ESMs are less effective at
51 simulating regional climate information due to their generally coarse resolution, which
52 currently ranges from 100 to 200 km for the atmospheric component and
53 approximately 100 km for the oceanic component (Bao et al. 2015). Hostetler et al.

54 (2011), for instance, showed that global spatial patterns and gradients of air
55 temperature can generally be captured by GCMs, while those of precipitation are not
56 resolved as satisfactorily. Most GCMs tend to overestimate precipitation levels for the
57 western region of North America while underestimating levels for the eastern region
58 of North America. Mehran et al. (2014) validated the Coupled Model Intercomparison
59 Project Phase 5 (CMIP5) GCMs against Global Precipitation Climatology Project (GPCP)
60 precipitation data and concluded that CMIP5 GCMs are in good agreement with GPCP

61 data in several areas but not for arid and certain sub-continental regions such as
62 northern Eurasia and eastern Russia. CMIP5 GCMs generally exhibit limited ability to
63 simulate high quartiles of precipitation and overestimate precipitation levels for
64 regions characterized by complex topography. Based on a gridded observational
65 extreme index dataset HadEX2, Sillmann et al. (2013) showed that CMIP5 GCMs are
66 able to simulate climate extremes and related trend patterns. They also suggested
67 using reference datasets carefully when evaluating climate model simulations in terms
68 of extremes indices while considering significant sources of uncertainty among
69 reference datasets.

70 Climate changes, especially in the case of extreme climate change, generally
71 feature high levels of spatial and temporal variability. A better understanding of
72 regional climate characteristics with a focus on the frequency and intensity of extreme
73 events and related changes is of vital importance to climate risk assessments as well
74 as adaptation implementation for regional communities. A better representation of
75 these local specifications can typically be obtained through either empirical-statistical
76 downscaling (ESD) or dynamical downscaling. The latter generally uses regional
77 climate models (RCMs) driven by GCM output or reanalysis data to derive regional
78 climate information. Regional climate modelling was pioneered by Giorgi and Bates
79 (1989) and has been widely used in climate change and extreme climate event studies
80 conducted at regional and local scales. From high spatial resolutions of limited areas,
81 RCMs can capture physiographic features such as coastlines, mountains and surface
82 characteristics in great detail and can consequently reproduce fine scale atmospheric

83 processes and features and especially for regions along coasts and with complex
84 topographical characteristics (Feser et al. 2011; Li et al. 2016; Li 2017; von Storch et al.
85 2017).

86 East Asia is one of the most vulnerable regions to climate change due its various
87 terrestrial features, complex climate system, and very high population density. The
88 region is greatly influenced by monsoon systems, which are typically accompanied by
89 the occurrence of extreme events such as tropical cyclones, floods and droughts. In
90 past years, several studies have been conducted on the climate changes over East Asia
91 based on observations or models (Liu et al. 1994; Gao et al. 2002; Fu et al. 2005; Zhang
92 et al. 2009; Kusunoki et al. 2011; Zou and Zhou 2013; Ji and Kang 2015; Kumar et al.
93 2015; Wu et al. 2016; Zou et al. 2016; Zhou et al. 2016; Um et al. 2017; Xie et al. 2017).

94 Observation results reveal that mean annual temperatures and heat wave frequencies
95 for most regions of East Asia have increased since the middle of the 20th century, while
96 precipitation trends, including those of extreme precipitation, show strong levels of
97 spatial variability (IPCC 2014). Studies have indicated that CMIP5 GCMs can
98 satisfactorily reproduce spatial patterns and interannual variability in surface
99 temperatures for China, while this is not the case for precipitation (Guo et al. 2013;
100 Huang et al. 2013; Chen and Frauenfeld 2014). Lee and Hong (2014) revealed that
101 increasing the spatial resolution of the RCM improves simulated precipitation and
102 temperature results and extreme event features for Korea. They also found that the
103 added value of an RCM is more evident for precipitation patterns than for temperature
104 patterns. However, Ji and Kang (2015) found that regional climate model RegCM4

105 simulates temperature extremes more accurately than precipitation.

106 In recent decades, many climate studies based on dynamical downscaling for East

107 Asia have been conducted based on the framework of the Regional Climate Model

108 Inter-comparison Project (RMIP) for Asia to improve our understanding of climatic

109 patterns of the East Asian monsoon region and to provide reliable regional climate

110 scenarios (Fu et al. 2005; Niu et al. 2015; Tang et al. 2016; Wu et al. 2016). Niu et al.

111 (2015) found that RCMs outperform the driving GCM in reproducing the summer mean

112 precipitation distribution and annual cycle for China, while deficiencies in simulating

113 summer precipitation are mainly attributed to limited capacities to reproduce low-

114 level circulation. Wu et al. (2016) showed that the RCM ensemble mean is superior in

115 reproducing both total and extreme summer precipitation relative to each individual

116 RCM.

117 Recently, a globally coordinated downscaling framework called the COordinated

118 Regional Downscaling Experiment (CORDEX, Giorgi et al. 2009), an initiative of the

119 World Climate Research Programme (WCRP, 2009), was established to further advance

120 RCM development, evaluation, analysis and application. Ensembles of dynamical or

121 statistical models driven by multiple CMIP5 GCMs have been created or are currently

122 under way for multiple regions throughout the world

123 (<http://www.cordex.org/community/domains.html>). Within the CORDEX-East Asia

124 domain (CORDEX-EA), several efforts have been undertaken to study mean climates

125 and extreme changes under the international CORDEX framework (Wang et al. 2013;

126 Lee et al. 2014; Oh et al. 2014; Huang et al. 2015; Zou et al. 2016; Park et al. 2016).

127 Huang et al. (2015) showed that the ensemble mean of RCMs can reasonably
128 simulate seasonal means, annual cycles, and inter-annual variability in precipitation,
129 while individual RCMs generate significant biases for some sub-regions and seasons.

130 Zou et al. (2016) showed that a regional ocean-atmosphere coupled model
131 outperforms an uncoupled RCM in simulating spatial patterns of low-level monsoon
132 flows crossing East Asia and the western North Pacific. Park et al. (2016) evaluated the
133 performance of multiple RCMs in simulating summer climate extremes of the CORDEX-
134 EA and demonstrated that RCMs present systematic biases in both seasonal means
135 and extremes of air temperature and precipitation. Their inter-RCM analysis reveals a
136 close relationship between model capacities to determine means and extreme values.

137 Previous studies have revealed the importance of multi-model ensembles in
138 modeling regional climate statistics and climate change. However, many studies have
139 been based on either a single GCM or RCM model (Brown et al. 2015; Gao et al. 2012a)
140 or on several RCMs driven by the same GCM of CMIP3 (e.g., Niu et al. 2015; Um et al.
141 2017; Wu et al. 2016). Furthermore, most studies have used only one observation
142 dataset for reference without considering uncertainties among observation datasets.
143 Considerable uncertainties found among observation products have been revealed by
144 many studies of the global landmass (e.g., Fekete et al. 2004) and of specific regions
145 (e.g., Xie et al. 2007). The effects of these uncertainties on the assessment of model
146 performance must be seriously considered.

147 In the present study, the performance of the regional climate model CCLM driven
148 by various CMIP5 GCMs was evaluated against several temperature and precipitation

149 observation or reanalysis datasets. Uncertainties generated from the use of different
150 driving GCMs together with the added value of dynamical downscaling were assessed
151 for the present period for both mean climate and extreme values. The influence of
152 observation uncertainties on model performance is discussed as well.

153 The paper is organized as follows: Section 2 describes the experimental setups and
154 datasets used. Section 3 presents our evaluation results of model performance in
155 simulating seasonal mean air temperatures, climatology and variability of precipitation
156 as well as large-scale circulation. Section 4 describes the capacity to which the CCLM
157 can simulate extreme precipitation patterns. Section 5 presents a summary and
158 concluding remarks.

159 **2. Experimental setups and datasets**

160 **2.1 Model description and simulation setups**

161 Non-hydrostatic regional climate model COnsortium for Small-scale MOdelling in
162 CLimate Mode (COSMO-CLM or CCLM, Rockel et al. 2008) version 5.0 is used in this
163 study. It is the climate version of the operational weather forecast model COSMO,
164 which was developed by the German Weather Service (DWD). The model is based on
165 Navier-Stokes primitive equations that describe non-hydrostatic compressible flows in
166 a moist atmosphere. The equations are solved on an Arakawa-C grid within a rotated
167 geographical coordinate system and with a generalized terrain-following height
168 coordinate (Schättler et al. 2008).

169 The CCLM has been used in climate studies for many regions worldwide (Rockel

170 and Geyer 2008). It has been used in several international projects (e.g., the Prediction
171 of Regional scenarios and Uncertainties for Defining EuropeaN Climate change risks
172 and Effects (PRUDENCE, Christensen et al. 2007), ENSEMBLES (Van der Linden et al.
173 2009) and the European branch of the World Climate Research Program Coordinated
174 Regional Downscaling Experiment (EURO-CORDEX, Jacob et al. 2005) of the Global
175 Energy and Water Cycle Experiment (GEWEX, <https://www.gewex.org/>) and its
176 successor CORDEX (Giorgi et al. 2009)).

177 In the present study, the model domain of the CCLM is set to the CORDEX-Region
178 7 East Asia (Fig. 1) among CORDEX initiatives (Giorgi et al. 2009). The horizontal
179 resolution is set to 0.44° with 223×187 grid points established in the longitudinal and
180 latitudinal directions, respectively. The temporal integration of the simulations is
181 carried out using the Runge-Kutta scheme with a timestep of 300 seconds. Ten grid-
182 boxes are set as a sponge zone at each lateral boundary. Given the substantial
183 extension of troposphere height across the tropical region, we set the lower boundary
184 of the Rayleigh damping layer in the model at 18 km rather than at the typical value of
185 11 km to avoid generating unrealistic results (Dosio et al. 2015). There are 45 vertical
186 levels with the top of the model domain at 30000 m in height.

187 Regional climate simulations of the CORDEX-EA were conducted for the current
188 climate period of 1950 – 2005 by downscaling from four CMIP5 GCMs (see Table 1):
189 the CNRM-CM5 (Volodire et al. 2013), EC-Earth (Hazeleger et al. 2010), HadGEM2
190 (Collins et al. 2011) and MPI-ESM-LR (Giorgetta et al. 2012). According to Mcsweeney
191 et al. (2015), the CNRM-CM5, HadGEM2 and MPI-ESM-LR are suitable GCMs for

192 generating downscaled climate for three sub-regions, i.e., Southeast Asia, Europe and
193 Africa. The performance of the EC-Earth, though not as satisfactory, is considered
194 acceptable in representing regional large-scale circulation and annual cycling features
195 of temperature and precipitation.

196 Various physical parameterization schemes (Table 2, left column) were used in the
197 simulations, including the Tiedtke mass-flux convection scheme (Tiedtke 1989), the
198 prognostic turbulent kinetic energy (TKE) closure scheme, the TERRA multi-layer
199 scheme for land surface processes (Schrodin and Heise 2002), and the radiation
200 scheme with full cloud-radiation (Ritter and Geleyn 1992). The PrEProcessor (PEP) tool
201 of the CCLM software package was used to generate invariant external forcing data
202 (Table 2, right column) (e.g., surface height, roughness length and soil).

203 **2.2 Datasets and statistical indices**

204 In considering the uncertainties of the reference datasets and their effects on
205 model performance, three latest reanalysis datasets and five observation datasets
206 (Table 3) were used to evaluate the quality of the CCLM results and to assess their
207 added values to the forcing GCMs. For the precipitation evaluations, Global
208 Precipitation Climatology Project (GPCP, Huffman et al. 2001), Global Precipitation
209 Climatology Center (GPCC, Schneider et al. 2014), Tropical Rainfall Measuring Mission
210 (TRMM, Huffman et al. 2007), Asian Precipitation-Highly Resolved Observational Data
211 Integration Towards the Evaluation of Water Resources (APHRO, Yatagai et al. 2012)
212 and Climatic Research Unit (CRU, Harris et al. 2014) data were used; the CRU, ERA-
213 Interim reanalysis (ERAI, Dee et al. 2011), JRA55 reanalysis (Kobayashi et al. 2015) and

214 MERR2 reanalysis datasets (Gelaro et al. 2017) were used for temperature evaluations.

215 To draw comparisons, coarse-resolution GCMs, reanalysis datasets and

216 observation datasets were interpolated to the CCLM grid (0.44° resolution) via bilinear

217 interpolation. Periods of available observations vary amongst the datasets, and the

218 period for each dataset is given in Table 3. It should be noted that the CORDEX-EA

219 region is not fully covered by the TRMM precipitation dataset. The following statistical

220 results related to the TRMM precipitation dataset are limited to the region covering

221 50°S to 50°N .

222 To investigate spatial variations in model performance, several land sub-regions

223 (shown in Fig. 1) are defined for the CORDEX-EA domain based on Zou et al. (2016).

224 To assess model performance in reproducing climatological patterns and

225 temperature and precipitation extremes, several statistics are used, including the

226 climatological mean (MEAN), mean bias (BIAS), spatial correlation (CORR), standard

227 deviation error (STDE) and added value index (AVI). Here, the STDE is defined as

228 variability in the error around its mean (c.f. von Storch and Zwiers 1999) and is written

229 as:

$$230 \quad \text{STDE} = \sqrt{RMSE^2 - BIAS^2} = \sqrt{\frac{1}{N} \sum_{i=1}^N (x'_i)^2 - (\frac{1}{N} \sum_{i=1}^N (x'_i))^2}$$

231 where N denotes the number of valid pairs of simulated and observed variables

232 determined spatially and where x'_i is the deviation between counterparts of the

233 simulated and observed variable.

234 The AVI is defined following Dosio et al. (2015) as:

235

$$\text{AVI} = \frac{(X_{GCM} - X_{OBS})^2 - (X_{CCLM} - X_{OBS})^2}{\text{Max}((X_{GCM} - X_{OBS})^2, (X_{CCLM} - X_{OBS})^2)}$$

236 where X_A denotes the seasonally averaged variable of dataset A. The AVI value
 237 ranges from -1 to 1: a positive AVI, when the squared error of the CCLM dataset is
 238 smaller than that of the GCM dataset, denotes an added value from dynamical
 239 downscaling and vice versa.

240 **3. Mean climatology and the added value of dynamical downscaling**

241 In this section, we thoroughly assess the capacity of the CCLM to reproduce
 242 principal features of East Asian climatology for the summer (June–July–August, JJA)
 243 and winter (December–January–February, DJF). We first evaluate the quality and
 244 added value of mean downscaled 2-m temperature and precipitation with respect to
 245 forcing GCMs by means of a spatial and temporal statistical analysis. Second, the
 246 performance of the CCLM in representing precipitation climate features is analyzed in
 247 detail in terms of annual cycles and intensity distributions. We also compare different
 248 observation (reanalysis) datasets against the reference dataset to quantify
 249 uncertainties in observations and their potential influence on the assessment of model
 250 performance. Finally, we quantify the capacity of the CCLM to resolve low-level
 251 circulation and its influence on the modeling of precipitation.

252 **3.1 Temperature climatology**

253 Figs. 2 and 3 show the spatial distributions of mean biases of modeled 2-m
 254 temperature for the winter and summer and the added value index for the period
 255 1979/12-2005/11. The reanalysis datasets (Figs. 2b-d) present significantly positive
 256 winter temperature biases (3-7 °C) for Mongolia (MG) and part of northeastern China

257 (NE). For the other regions biases mostly range from -3 to 3 °C. Winter 2-m
258 temperatures are generally underestimated compared to CRU values for 3 of 4 GCMs
259 (Figs. 2e-h) and to up to 5 °C for most regions such as southern (SC) and western China
260 (WC), India, the Indo-China Peninsula, and the Maritime Continent. This
261 underestimation can reach very large values (9 °C) for the Tibetan Plateau and
262 especially when using the CNRM-CM5 (Fig. 2e). In contrast, the MPI-ESM-LR (Fig. 2h)
263 presents strong overestimations for China and MG. All the CCLM results (Figs. 2j-n)
264 overestimate observed winter 2-m temperatures for MG and for part of northwestern
265 China. Areas for which the CCLM_MPI-ESM_LR (Fig. 2m) overestimates simulated
266 temperature are larger than those shown by the other three CCLM simulations, which
267 is consistent with their GCM counterparts.

268 In analyzing the geographical distribution of the added value index, for the winter
269 (Figs. 2o-s), we note that positive AVI distributions share consistent features among
270 simulations and mainly cover India and parts of northwestern China. The CNRM-CM5
271 and HadGEM2 driven simulations (Figs. 2o, q) show larger fractions of the CORDEX-EA
272 domain with positive AVI values compared to the other two simulations. Added value
273 distributions can also be observed from GCM and RCM ensemble mean results (Fig.
274 2s). Furthermore, we note that deterioration as a result of downscaling is mainly
275 observed for the Tibetan Plateau, for Mongolia and for areas of coastal China for which
276 temperature biases generated by CCLM simulations are more significant than those
277 generated by GCMs. However, it is evident that large temperature biases of CCLM
278 simulations for some of these regions are comparable to those of reanalysis datasets

279 (Figs. 2b-d). Furthermore, strong negative biases observed from CCLM simulations of
280 WC (Figs. 2j-n) mostly fall within the range of observation uncertainty (see Fig. S1e),
281 implying acceptable simulated results by the CCLM.

282 Model biases in 2-m mean temperatures for the summer (Fig. 3) differ
283 considerably from those for the winter. The biases of reanalysis datasets mostly range
284 from -3 to 3 °C with a positive bias found for the East Asian continent and with a
285 negative bias found for the Maritime Continent. Furthermore, from several
286 observation datasets we find considerable levels of observation uncertainty for the
287 Tibetan Plateau (see Fig. S2). The standard deviation between observations can exceed
288 a value of 3 °C. GCMs generally show biases from -3 °C to 3 °C; among them, HadGEM2
289 presents the largest fraction of the CORDEX-EA domain with a positive bias. From our
290 CCLM simulations, we observe positive biases that are greater than corresponding
291 GCM values for several regions. However, the bias of spatial distributions between the
292 GCM and corresponding CCLM run is generally consistent.

293 The geographical distribution of the AVI (Figs. 3o-s) is rather heterogeneous
294 without presenting noticeably consistent patterns between different GCM-RCM
295 combinations. Furthermore, the models' ensemble means (Figs. 3i, n, s) do not present
296 obvious signs of added value when comparing downscaled results to those of the
297 driving GCMs. The absolute biases of GCMs and CCLMs are generally less significant
298 than the corresponding biases for the winter (Figs. 2i, n). A comparison of Fig. 2 and
299 Fig. 3 reveals considerable seasonal variability in bias values and added value
300 distributions for 2-m temperatures with less significant biases for the summer but

301 larger areas for which the AVI is positive for the winter.

302 Using various statistical metrics, we further evaluate the performance of GCMs,

303 CCLM simulations, corresponding ensemble means and three reanalysis datasets in

304 reproducing the 2-m temperature climatology of different land sub-regions and of the

305 entire land area (i.e., all land points of the CORDEX-EA domain) for the winter and

306 summer (Fig. 4). This analysis further confirms our findings that temperature

307 underestimations are widely distributed for the winter but not over the MG and

308 Korean Peninsula and Japan (KJ) for GCMs and that summer biases are much less

309 significant than those for the winter for both GCM and CCLM runs. An area-averaged

310 bias is found at within ± 2 °C for the summer for most sub-regions. Reanalysis datasets

311 reveal considerably positive biases for the winter for the MG (and for the NE and KJ for

312 the ERAI), where GCMs and CCLM simulations do not perform realistically.

313 In terms of spatial correlation distributions, we note that values are mostly larger

314 than 0.9, while correlations are relatively lower for the MG region for the winter and

315 for the KJ region for the summer. From ensemble mean results, we find a clear

316 improvement in spatial correlations by downscaling all sub-regions for the summer,

317 which is not the case for the winter. Figs. 4e-f show that the error variance for 2-m

318 temperatures of GCM and CCLM simulations is smaller for the summer than for the

319 winter for the MG, NE, KJ and land regions. STDE values are mostly less than 2.5 °C for

320 the summer for most sub-regions except for those of the WC, while in winter model

321 results show error variances exceeding values of 3 °C for regions such as the WC and

322 MG. Additionally, consistent error variance reduction is achieved by downscaling the

323 KJ region for both seasons. STDE values of the reanalysis datasets are less than those
324 of the GCMs and CCLM simulations for most cases, but they still present uncertainties
325 among regions, seasons and datasets of 0.5 to 2.5 °C.

326 **3.2 Precipitation climatology**

327 Figs. 5 and 6 show spatial distributions of mean biases of modeled precipitation
328 for the winter and summer and the added value index for the period 1996/12 –
329 2005/11. Based on the GPCP climatological mean, we present two prominent rainfall
330 bands for the winter: one located over the tropical region around the Equator
331 (rainband 1) and another positioned over the northwestern Pacific region, east to
332 Japan (rainband 2). Precipitation intensities measured for the central areas of these
333 two rainbands exceed values of 6 mm/day. TRMM data generally show higher rainfall
334 levels for rainband 1 by 1-3 mm/day and show less rainfall for the rainband 2 by 1-
335 3 mm/day. Across the land areas (Figs. 5b-e), observation uncertainties are mainly
336 found for the Maritime Continent and for Japan by generally less than 3 mm/day;
337 however, the APHRO can underestimate GPCP values for the Maritime Continent by
338 more than 5 mm/day.

339 According to the modeled results, rainband 1 precipitation occurring over water
340 bodies is generally overestimated by the GCMs and by CCLM simulations and
341 especially by the HadGEM2 and MPI-ESM-LR (Figs. 5f-o). However, most CCLM
342 overestimations for rainband 1 are greater than those of the driving GCMs with values
343 reaching in excess of 11 mm/day. GCM and CCLM results generally underestimate
344 precipitation levels for rainband 1 over land areas with the latter generally making a

345 more significant underestimation than the former. Precipitation occurring over
346 rainband 2 is generally underestimated by the GCMs to values of up to -3 mm/day with
347 the exception of the CNRM-CM5, which overestimates it. Bias observed over rainband
348 2 is reduced by the CCLM as shown in Figs. 5k-o. A comparison of ensemble mean
349 biases (Figs. 5j, o) shows that both GCM and CCLM ensemble means generally
350 outperform individual model runs.

351 In terms of added value from downscaling, we see generally consistent spatial
352 patterns of AVI distributions for different GCM-CCLM combinations. Over the
353 equatorial areas, there is generally deterioration (a negative AVI) of climatological
354 means of precipitation for CCLMs. However, across rainband 2, the Japan Sea, Chinese
355 marginal seas, eastern China, and a large part north to China, AVI values are positive,
356 implying that the CCLM can add value to GCMs in terms of precipitation climatology.
357 However, we must note that this added value may be attributed to the referred
358 observations, as we found that for northern regions reaching 20 °N, both the GCM and
359 CCLM can realistically reproduce winter means of observed precipitation from the
360 TRMM bias relative to the GPCP (Fig. 5b). The added value derived by downscaling
361 may not be significant relative to observation uncertainties.

362 For the summer, GPCP observations (Fig. 6a) show strong patterns of precipitation
363 (over 6 mm/day) widely distributed across the CORDEX-EA domain except for the WC
364 and MG and for part of the Pacific Ocean. Observed precipitation levels are particularly
365 intense (over 15 mm/day) along the west flank of the Indo-China Peninsula. We find
366 that uncertainties of the observed precipitation datasets are more pronounced than

367 those for the winter and especially for the Tibetan Plateau, Indo-China Peninsula and
368 Maritime Continent (Figs. 6b-e). The GCMs show similar patterns of negative biases
369 (Figs. 6f-o) extending from India and the Indo-China Peninsula to southern China (SC),
370 KJ. Differences are found as well; we find positive biases in HadGEM2 and MPI-ESM-
371 LR mainly for water bodies positioned between equator and 30°N, while this is not the
372 case for the other two GCMs. Some common features of bias distributions are found
373 between the CCLM simulations: a strong positive bias over the northwestern Pacific
374 Ocean between the equator and 30 °N and mostly weak negative biases for southern
375 and eastern China, the East China Sea and the Korean Peninsula. Added value is found
376 for Japan and large water regions surrounding Japan for all GCM-CCLM combinations
377 (Figs. 6p-t). For the other regions degrees of added value vary from simulation to
378 simulation. MPI-ESM-LR combinations show positive AVI values for the largest fraction
379 of the CORDEX-EA domain.

380 In comparing Figs. 5 and 6, we find that CNRM-CM5 and EC-EARTH outperform
381 the other two GCMs in reproducing levels of precipitation intensity for the winter and
382 summer and especially for tropical water regions. This feature is partly inherited by
383 corresponding downscaled simulations, which implies that boundary forcing has
384 considerable influence on downscaled results. At the same time, similarities in spatial
385 distribution patterns observed between CCLM simulations are enhanced by
386 downscaling when compared to those of GCMs.

387 As for the 2-m temperatures, several statistical metrics were used to assess the
388 performance of the examined models in representing precipitation patterns observed

389 across different sub-regions for the winter and summer (Fig. 7). Biases found for the
390 winter are much less significant than those found for the summer. In the selected sub-
391 regions and land areas for the winter (Fig. 7a), bias values are generally negative for
392 GCMs at -0.25 to -1 mm/day, while they are mostly positive for CCLM simulations (0.25
393 to 0.6 mm/day). SC and KJ and the average of land areas show a reduction in winter
394 biases as a result of downscaling based on the ensemble mean. In the summer, biases
395 are generally negative except for those for the WC and MG regions. Negative biases
396 are the largest for the SC and KJ regions. Bias reduction is also found for the NE, KJ and
397 land areas. Furthermore, we find levels of observation uncertainty to be greater for
398 the summer than for the winter and especially for the WC, SC and KJ, for which GCMs
399 and CCLM simulations generally perform unrealistically.

400 Spatial correlation coefficients between modeled and observed precipitation (Figs.
401 7c-d) are lower than those for 2-m temperatures (Figs. 4c-d); correlation values are
402 mostly greater than 0.5 but vary from region to region. In the case of the MG region,
403 CORR values are greater for the summer than for the winter and vice versa for the KJ
404 region. Downscaling adds hardly any value to spatial patterns of climatological
405 precipitation found for both the summer and winter. Error variances for the winter are
406 generally smaller than those for the summer. In most cases, values are less than
407 0.8 mm/day for the winter for selected sub-regions while varying strongly from region
408 to region for the summer with smaller error variances found for the MG and NE regions
409 than for the other regions. Furthermore, it can be seen that downscaling hardly
410 contributes to the error variance reduction of modeled precipitation. However, values

411 are comparable to those of other observation datasets in terms of the error variances
412 of most sub-regions for the winter (Figs. 7e-f).

413 In summarizing our analysis, we note considerable seasonal variability in spatial
414 distributions of 2-m temperature biases and in added value from CCLM simulations:
415 biases are generally smaller for the summer than for the winter, but areas with added
416 value are larger for the winter. Added value in the winter is mainly found for India and
417 part of northwestern China across all GCM-CCLM combinations. The CNRM-CM5 and
418 HadGEM2 driven runs show larger areas for which added value can be found relative
419 to the other two combinations found for the winter. For precipitation levels,
420 downscaling can add value to GCMs by reducing the bias of part of the domain, but
421 the CCLM hardly outperforms GCMs when applied to tropical regions where extreme
422 rainfall patterns are observed. The bias distributions of downscaled runs can be partly
423 inherited from their corresponding GCMs for both variables. At the same time,
424 similarities found between downscaled simulations are more significant than
425 similarities observed between forcing GCMs and especially in the case of summer
426 precipitation (Fig. 6).

427 **3.3 Precipitation variability and intensity distribution**

428 According the results shown in Fig. 8, we note that observation datasets (GPCP,
429 GPCC, CRU, APHRO and TRMM) are generally consistent in capturing annual cycles of
430 precipitation with the largest values found for the summer and with the lowest values
431 found for the winter across all regions. In particular, SC and KJ regions show the most
432 intense rainfall peaks in the summer relative to those of the other regions.

433 Discrepancies between observations are found. The APHRO shows less rainfall than
434 the other observations for the summer and particularly when considering the whole
435 land area (Fig. 8g).

436 The annual precipitation cycle of the KJ region is less satisfactorily simulated by
437 the models especially for the period of July to September, for which both GCM and
438 CCLM simulations show underestimations of more than 2.5 mm/day. Although all of
439 the models exhibit a general capacity to reproduce the general structure of the annual
440 cycle, the models' capacities to represent precipitation intensity vary considerably. For
441 GCMs, the MPI-ESM-LR generates the worst results, as it underestimates precipitation
442 levels for almost all of the selected regions. The CNRM-CM5 and HadGEM2 are
443 generally consistent and are superior to the EC-EARTH in capturing annual cycle
444 variability in precipitation for regions such as the MG, SC and NE and for the whole
445 land area.

446 For the CCLM, downscaled simulations most closely reflect observations (except
447 for the APHRO) than their GCM counterparts for the whole land area (Fig. 8 g) with the
448 exception of that of the HadGEM2 GCM-CCLM combination for May to August.
449 Regarding annual cycle variability of sub-regions, the added value is found to be
450 generated by the CCLM_MPI-ESM-LR and MPI-ESM-LR for all regions except for the SC
451 and northern China (NC) regions for the summer. CCLM_CNRM-CM5 performs worse
452 than the CNRM-CM5 in the WC, MG, NC and KJ; it outperforms or performs similar to
453 the CNRM-CM5 in terms of NE (Oct. to Dec.) and SC (winter half year). The CCLM-
454 HadGEM2 adds value to its forcing HadGEM2 over KJ in the winter half year.

455 Deterioration or no obvious improvement by CCLM-HadGEM2 to HadGEM2 in the
456 other sub-regions. The EC-EARTH is closer to observations than CCLM_EC-EARTH in
457 WC. However, their performance varies by region and season without showing
458 consistent patterns in added value for the other sub-regions.

459 The box and whisker plots in Fig. 9 and Fig. 10 show distributions of land-area-
460 averaged daily precipitation for each sub-region for the winter and summer,
461 respectively. GPCP observations show that the winter is an arid season for much of the
462 CORDEX-EA region, although considerable variability is found across regions; for
463 instance, the KJ is subject to the heaviest rainfall (both the maximum and 95th
464 percentiles of precipitation) with maximum daily rainfall levels exceeding 25 mm/day;
465 on the other hand, the MG is the driest region with daily precipitation levels of less
466 than 1.5 mm/day. The range of the precipitation distribution, which is denoted from
467 the distance between the 25th and 75th percentiles, is narrower than or around
468 approximately 0.5 mm/day for all sub-regions except for the SC and KJ regions. TRMM
469 rainfall is generally consistent with GPCP in reflecting precipitation distributions for
470 most of the examined regions. Some differences in maximum rainfall levels are
471 observed for the SC, NC and KJ. GCMs hardly reproduce these features of daily
472 precipitation distributions for almost all of the sub-regions.

473 Extreme rainfall patterns are largely underestimated by GCMs with the range of
474 simulated daily precipitation typically being much narrower than observed ranges,
475 especially for the MG, NC and NE. Of the GCMs examined, the MPI-ESM-LR is the worst
476 in representing observed precipitation distributions. In comparison, CCLM simulations

477 add value to GCMs in representing precipitation distributions. The intensities of
478 extreme precipitation simulated by CCLMs generally reflect GPCP observations better
479 than that of GCMs. The spatial variability of observed extreme rainfall levels is also
480 better reproduced by the CCLM than by GCMs. The precipitation range of CCLM
481 simulations is in better agreement with observations than those of GCMs. No CCLM
482 simulation can outperform the other simulations for all sub-regions, but we note that
483 the CCLM_HadGEM2 is the best of the GCM and CCLM runs in capturing GPCP winter
484 rainfall distributions for land regions (Fig. 9g), and the improvement by CCLM for MPI-
485 ESM-LR combination is more apparent than those for other combinations.

486 In contrast, the summer is the rainy season for the CORDEX-EA region.
487 Precipitation intensity levels vary strongly from region to region (Fig. 10). Features of
488 the GPCP and TRMM are generally similar across most sub-regions. For the selected
489 sub-regions, SC and KJ are characterized by the highest maximum precipitation levels
490 (greater than 30 mm/day). MG is the most arid region in the summer as in the winter,
491 with area-mean maximum precipitation levels reaching 8 mm/day. The precipitation
492 range is much broader in the summer than in the winter. The land-area-averaged daily
493 precipitation (Fig. 10g) generally ranges from 3 mm/day to 6 mm/day. The
494 precipitation distribution of GCMs is in better agreement with observed precipitation
495 in the summer than that in the winter for the MG, NC and NE regions. As was found in
496 the winter season, the MPI-ESM-LR is generally the least effective at simulating
497 precipitation distributions among the GCMs. CCLM_MPI-ESM-LR also ranks as the least
498 effective of the CCLM simulations, but it adds value to MPI-ESM-LR for most regions.

499 CCLM simulations are in better agreement with observations than GCMs in
500 reproducing extreme or precipitation ranges for the NC, NE, KJ and land regions, which
501 is not found to be the case for the other sub-regions.

502 **3.4 Large-scale circulation in the lower troposphere**

503 The amount of water vapor is generally linked to the atmosphere's potential
504 capacity for precipitation (Zhou and Yu 2005). To investigate mechanisms that may
505 control precipitation climatological mean bias and seasonal variability, we compared
506 seasonal means of the modeled water vapor mixing ratio (RV), wind vectors and water
507 vapor transport in the lower troposphere at 850 hPa to those derived from ERA-
508 interim reanalysis data (ERAI) for the winter (Fig. 11) and summer (Fig. 12).

509 Fig. 11a shows that water vapor mixing ratios generally decrease from the equator
510 to high latitudes in the winter, exceeding values of 10 g/kg for the tropical region and
511 measured at less than 2 g/kg for most northern regions to 30 °N. The spatial
512 distribution of the winter mean water vapor mixing ratio is similar to that of GPCP
513 mean precipitation (Fig. 5a). For the summer (Fig. 12a) we find that the water vapor
514 mixing ratio generally intensifies (to over 12 g/kg in regions lying between 10 °N and
515 30 °N) and shifts northward relative to that of the winter. At the same time, the rainfall
516 band moves northward (Fig. 6a) and covers similar regions as those of the water vapor
517 mixing ratio. This result indicates that water vapor levels set the basis of seasonal
518 variability in precipitation climatological means, which is further verified by the large
519 spatial correlation coefficient found (of generally larger than 0.6) between seasonal
520 mean precipitation and water vapor amount for observations or model data (now

521 shown here).

522 Reanalyzed winter features of the water vapor mixing ratio and large scale
523 circulations are generally satisfactorily simulated by all four CCLM simulations for
524 northern land regions to 30°N, while this is not the case for tropical regions, for which
525 significant biases in water vapor and wind speed values are generally found (Figs. 11b-
526 e). Large wind biases are also found for regions northeast to Japan. The overestimated
527 air pressure found for the Tibetan Plateau and for the northwestern Pacific Ocean east
528 to Japan and underestimated air pressure found for tropical regions are supposed to
529 result in the biased winds especially over water regions (see Fig. S3).

530 In addition, it can be observed that winter precipitation biases of the CCLM
531 simulations (Figs. 5k-o) are closely related to biases of water vapor transport (Figs. 11f-
532 i); overestimated precipitation for some tropical regions is mainly a result of an
533 overestimated convergence of water vapor transport found for tropical regions in all
534 CCLM simulations. CCLM_HadGEM2 outperforms the other CCLM simulations for
535 some tropical regions in terms of water vapor mixing ratios, wind fields and water
536 vapor transport, thus performing the best of the CCLM simulations in generating
537 winter precipitation patterns (Fig. 5) for these regions.

538 In the summer, precipitation in East Asia is derived from three main sources (Fig.
539 12a): 1) strong southwesterly winds from the Indian summer monsoon; 2) southerly
540 and southeasterly winds from the West Pacific and 3) cross-equatorial winds.
541 Simulated biases of low-level circulation will influence associated amount of water
542 vapor transport.

543 We find pronounced eastward and northeastward shifts in western Pacific
544 subtropical highs from our simulations (Figs. S4b-e). In addition, the pressure bias
545 patterns are generally consistent across all simulations (see Figs. S4g-j). A pattern of
546 positive (weak negative), strongly negative, and positive (weak negative) is observed
547 from north to south with a strong negative pressure bias found for regions spanning
548 the Tibetan Plateau-South China to the northwestern Pacific Ocean from 15 °N to
549 30 °N, generating apparent cyclonic wind biases (Figs. S4g-j). Biases in simulating large-
550 scale circulation and related water vapor transport result in rainfall underestimations
551 for South China and overestimations for regions ranging from the South China Sea to
552 the northwestern Pacific Ocean (Figs. 6k-o). Specifically, northeasterly biases over
553 South China derived from CCLM simulations (Figs. 12b-e) lead to lower levels of water
554 vapor transport and a negative precipitation bias found over South China (Figs. 6k-o).
555 A cyclonic wind bias (Figs. 12b-e) is supposed to cause overestimated the convergence
556 of water vapor transport (Figs. 12f-i) and associated overestimated summer
557 precipitation for regions spanning the South China Sea to the northwestern Pacific
558 Ocean (Figs. 6k-o).

559 As a short summary, we find strong spatial variability in CCLM simulations
560 reproducing low-level circulations and related water vapor transport processes. Less
561 optimal results are found for tropical regions for the winter and for the South China
562 Sea and northwestern Pacific Ocean for the summer, meaning that CCLM simulations
563 poorly reproduce precipitation climatological means for these regions. Limited
564 capacities to model western Pacific subtropical highs and associated cyclonic wind

565 biases for the summer are also found for some GCMs of the CMIP3 and CMIP5 (Feng
566 et al. 2014; Song and Zhou, 2014) and for RCM models (Niu et al. 2015). This scenario
567 may be a result of an unrealistic configuration of the Tibetan Plateau, with simulated
568 large biases in pressure systems derived for both the winter and summer (Figs. S3-S4),
569 which may heavily influence the climate modeling of (thermo-) dynamic processes for
570 the CORDEX-EA region (Wang et al. 2008). Model physics and parameterizations,
571 especially in terms of convection scheme selection may also greatly affect low level
572 circulation and precipitation modeling capacities (Niu et al. 2015).

573 **4. Climate extremes – precipitation relevant**

574 Extreme climate events have serious impacts on land and marine environments
575 and on human activities. These events involve high levels of spatial and temporal
576 variability, especially at regional or local scales. It is challenging yet important for
577 climate models to reproduce features of climate extremes. Here, the capacity of GCMs
578 and CCLM simulations to reproduce relevant precipitation extremes is assessed by
579 comparing them against GPCP observations for 1996-2005. Three precipitation-
580 relevant extreme climate indices drawn from a set of 27 extreme indices defined by
581 the Expert Team on Climate Change Detection and Indices (ETCCDI, Frich et al. 2009
582 and Zhang et al. 2011) are used: the simple daily intensity index (SDII, annual mean
583 precipitation measured for wet days at precipitation $\geq 1.0 \text{ mm/day}$), the consecutive
584 dry day (CDD, annual maximum number of consecutive days with precipitation <
585 1.0 mm/day) and the consecutive wet day (CWD, annual maximum number of

586 consecutive days with precipitation \geq 1.0 mm/day). We expect to find that high-
587 resolution CCLM simulations can add value to GCMs in simulating features of extreme
588 climate events.

589 Fig. 13 shows the spatial distribution of the observed SDII index, biases of GCM
590 and CCLM simulations against observations and the added value index. The figure
591 shows that the SDII generally exceeds a value of 4 mm/day over the CORDEX-EA
592 domain except for inner continental regions such as MG and WC. High SDII indexes
593 exceeding 12 mm/day are mainly found along coastal areas and in parts of the Pacific
594 and Indian Oceans. The intensity of observed SDII values is generally underestimated
595 by GCMs, especially by the CNRM-CM5 and EC-EARTH. The HadGEM2 and MPI-ESM-
596 LR generally underestimate observed SDII values for land areas, while they
597 overestimate SDII values for some tropical water regions. CCLM simulations share
598 similar distributions of SDII index biases. Overestimations of observed SDII intensities
599 by CCLM simulations are mainly found for NC, MG, the Himalayan region and most
600 water regions. Extreme overestimations of greater than 9 mm/day can be clearly
601 observed in tropical regions, especially in the case of CCLM_HadGEM2 and CCLM_MPI-
602 ESM-LR. Bias reductions achieved by downscaling are mainly found for regions
603 spanning India to Southeast Asia; extending north across eastern China, Korea, and
604 Japan and covering the Pacific Ocean east to Japan, which is also shown by positive
605 AVI values in Figs. 13 l-p.

606 The observed annual CDD index (Fig. 14a) presents periods of less than 20 days
607 mainly for the tropical region and northwestern Pacific region. A large part of the

608 CORDEX-EA features 20 - 60 consecutive dry days with the exception of MG, WC, India
609 and part of the western Pacific region, for which the CDD periods exceed 60 days.
610 There are similarity of CDD biases distributions among four GCMs. The biases are
611 obvious over regions with large observed CDD index. GCMs generally overestimate
612 observed CDD values for most land of the CORDEX-EA region while underestimating
613 CDD values for part of the western Pacific and South China Sea, which is also reflected
614 by GCM ensemble means (Fig. 14f). The MPI-ESM-LR is the least effective GCM in
615 reproducing CDD index distributions, which largely overestimate observed CDD for the
616 continental region of the CORDEX-EA. Downscaled results show both improvements
617 and decline relative to driving GCMs. Bias reduction and positive AVI (Figs. 14g-p)
618 derived through downscaling can be detected for land regions north to 30°N. Regions
619 exhibiting decline are mainly distributed across India, the Indo-China Peninsula, parts
620 of the SC and tropical water regions. The MPI-ESM-LR driven simulation (Fig. 14o)
621 features the largest regions with positive AVI values relative to those of the other three
622 simulations.

623 Finally, Fig. 15a shows that the observed annual CWD for tropical land regions and
624 for the west coast of the Indo-China Peninsula can exceed 40 days but are less than 15
625 days for regions north to 30°N. Northwestern China presents the lowest CWD values
626 (less than 5 days). CWD indices are generally overestimated by more than 20 days for
627 the region south to 30°N for the CNRM-CM5, EC-EARTH and HadGEM2. Biases of the
628 CWD index of the MPI-ESM-LR are much smaller than those of the other three GCMs.
629 Added value is achieved by downscaling in reproducing the CWD index (Figs. 15g-p).

630 Biases of the CWD index of downscaled results mostly fall within ± 20 days except for
631 those for some tropical regions and for part of the Tibetan Plateau. Spatial
632 distributions of the CWD index are very similar for the CCLM_EC-EARTH,
633 CCLM_HadGEM2 and CCLM_MPI-ESM-LR. Across all GCM-CCLM combinations, the
634 CNRM-CM5 GCM-CCLM combination (Figs. 15g, l) offers the most added value by
635 downscaling, while the MPI-ESM-LR GCM-CCLM combination (Figs. 15j, o) offers the
636 least amount of added value. The added value for the tropical region south to 20°N is
637 more apparent, presenting large observed CWD values (Fig. 15a), which are greatly
638 overestimated by GCMs (Figs. 15b-f).

639 **5. Summary and concluding remarks**

640 In the present study, several CCLM simulations were conducted over the CORDEX-
641 EA domain following CORDEX initiatives using four CMIP5 GCMs (CNRM-CM5, EC-
642 EARTH, HadGEM2 and MPI-ESM-LR) as forcing fields. The modeled outputs were
643 assessed against five observation datasets (i.e., GPCP, GPCC, CRU, TRMM and APHRO)
644 and three most current reanalysis datasets (ERA-Interim, JRA55 and MERRA2). We
645 address mainly three questions. First, can CCLM simulations realistically reproduce
646 general features of historical climatic patterns for the CORDEX-EA in terms of
647 temperature and precipitation (e.g., seasonal climatological mean, annual variability
648 and precipitation relevant extremes)? Second, can CCLM simulations add value to
649 forcing GCMs? Finally, how large is the uncertainty among observation/reanalysis
650 datasets and corresponding effects on model assessments?

651 It is found that the performance of downscaled results in reproducing
652 climatological features varies from region to region and is highly dependent on the
653 variable, season, metric and forcing GCM considered. In the winter, negative
654 temperature biases cover most regions except for the MG region, for which a
655 significantly positive temperature bias is found. In the summer, there are more areas
656 with a positive temperature bias are found. The bias intensities of modeled summer
657 temperatures are generally lower those of modeled winter temperatures, while more
658 areas are afforded added value by downscaling for the winter rather than for the
659 summer.

660 Regarding precipitation, downscaling simulations can add value to forcing GCMs
661 for part of the CORDEX-EA region and especially for the winter. However, they do not
662 outperform GCMs in reproducing heavy rainfall patterns for the tropics. The CNRM-
663 CM5 and EC-EARTH outperform the other two GCMs in reproducing intensities of
664 precipitation for both the winter and summer, especially for tropical water bodies as
665 found for corresponding downscaling simulations. A consistency of bias distributions
666 found between GCM and CCLM results indicates that biases of GCM forcings are partly
667 inherited by downscaled RCMs, denoting the significance of GCM boundary forcing for
668 downscaling. We find that similarities of spatial patterns of bias distributions among
669 CCLM simulations are much more significant than those of GCM results, revealing a
670 systematic bias resulting from CCLM dynamical processes or parameterization
671 schemes.

672 The structure of precipitation annual variability can be captured by all GCMs and

673 CCLMs. Four CCLM simulations except for the CCLM_HadGEM2 can add value to GCM
674 forcings in terms of the annual variability of land-area-averaged precipitation. However,
675 no consistent pattern of added value is found for sub-regions derived from CCLM
676 simulations. CCLM simulations are in better agreement with observations in
677 reproducing area-averaged daily precipitation distributions for the winter than GCMs,
678 especially in the case of MPI-ESM-LR GCM-CCLM combinations. However, no obvious
679 improvement results from downscaling to GCMs for the summer for area-averaged
680 daily precipitation distributions.

681 Concerning precipitation extremes, CCLM simulations show obvious added value
682 to GCMs in generating observed consecutive wet days (CWD index) for tropical regions.
683 We also find obvious added value from reproducing consecutive dry days (CDD index)
684 over land regions north to 30°N. Pronounced signs of improvement and deterioration
685 are observed when downscaling to GCMs in the case of the simple daily intensity index
686 (SDII). Furthermore, we found high levels of seasonal dependence for extreme
687 precipitation indices; spatial patterns of annual SDII and CWD indices mainly resemble
688 those of the summer, while spatial patterns of annual CDD index are greatly dependent
689 on winter CDD indices (not shown here). Further evaluations should perform more
690 detailed studies of seasonal rainfall extremes.

691 We note a considerable discrepancy among reanalysis datasets or observation
692 datasets in reflecting precipitation or temperature features for certain regions. Such
693 uncertainties can be as significant as typical biases of GCMs and CCLM simulations
694 (based on a specific observation dataset). For instance, we find a positive temperature

695 bias for Mongolia and for part of northeastern China for the winter from three
696 reanalysis datasets (Figs. 2b-d) and high levels of variability among observation
697 datasets of temperature climatological means for western China (Fig. S1 and Fig. S2),
698 and in summer precipitation means for part of the Tibetan Plateau and Maritime
699 Continent (Figs. 6b-e). This implies that though CCLM simulations may not be able to
700 add value to GCMs, simulated results for some (deterioration) regions can be
701 acceptable relative to those of reanalysis datasets or observation uncertainties. On the
702 other hand, the use of a different reference dataset may result in non-add value by
703 downscaling for some regions as is shown in Fig. 8 for annual variability in rainfall for
704 land areas using the APHRO as a reference. Therefore, a careful selection of reference
705 datasets is recommended not only when evaluating modeled climate extremes
706 (Sillmann et al. 2013) but also in terms of climate mean evaluations.

707 Furthermore, it should be noted that only one regional climate model CCLM was
708 used in the present study. Uncertainties related to using different RCMs to generate
709 climate features for East Asia were not investigated. From previous studies (Gao et al.
710 2012b; Niu et al. 2015; Gao and Chen, 2017; Zhou et al. 2016), we found that most
711 RCMs are able to capture general features of seasonal means and annual cycles of
712 surface temperature and precipitation. However, model performance varies across
713 sub-regions and seasons with similarities and differences found between models. Cold
714 and wet biases are derived from most RCMs in generating summer climates of the
715 Tibetan Plateau due to the limited applicability of modern land surface models to the
716 Tibetan Plateau region (Yang et al. 2005; Gao and Chen, 2017). Land surface schemes

717 regulate the vertical profiles of atmospheric temperature and horizontal patterns of
718 moisture advection, greatly determining the climatology and spatial patterns of
719 temperature and precipitation.

720 As shown from results of some RCMs (Huang et al. 2015), observed precipitation
721 is overestimated for the northwestern Pacific Ocean for the summer and for equatorial
722 regions in the winter. However, these results differ from those of CCLM simulations
723 conducted by Zhou et al. (2016). We found that these significant positive biases are
724 partially inherited from forcing reanalyses/GCMs, though the dynamic setups (regions,
725 physical parameterizations, and resolutions) of individual models are mainly meant to
726 contribute to generated biases.

727 To improve the capacity for the RCM to simulate regional climate features, it is
728 important to further advance the development of model physics and parameterization
729 schemes of both forcing GCM and RCM. On one hand, the misrepresentation of large-
730 scale features by forcing GCMs can be limited; on the other hand, advanced soil,
731 convection and other parameterization schemes used in RCM have potential to reduce
732 systematic biases of climatic features, which is particularly true for the tropics, where
733 small-scale convection patterns are an important process. The development and
734 optimization of convection scheme is supposed to be more significance for
735 improvement of tropical climate modelling than simply increasing model resolutions.

736 Specific attention should also be paid to the modeling of specific regions or circulation
737 systems such as the Tibetan Plateau and western Pacific subtropical high, which have
738 significant effects on the climate systems of East Asia and play an important role in

739 enhancing overall model performance. Efforts to optimize model setups (e.g., domain
740 size selection, sponge zones, or the adoption of spectral nudging) would also
741 contribute to the improvement of model results. Furthermore, we found that
742 ensemble means of GCMs and CCLM simulations outperform individual simulations in
743 reproducing climate features such as climatological means of winter precipitation. To
744 limit random errors and to assess model uncertainties in simulating climate features,
745 large-member ensemble simulations that consider different forcing GCMs, multi-RCMs
746 and multiple patterns of perturbed physics must be conducted.

747 In the present study, we mainly assessed the capacities and added value of RCM
748 in reproducing climatological means, variability and extreme indices of precipitation.
749 The capacity for the RCM to simulate short-term variability (e.g., diurnal cycles and
750 intra-seasonal variability) has not been investigated and would require the use of high-
751 resolution datasets. Model capacity to simulate temperature extremes and other
752 extreme rainfall events is also not considered. These issues require further
753 investigation.

754 **Acknowledgements**

755 Thanks to the three reviewers (Masato I. Nodzu and the other two anonymous
756 reviewers) for their constructive comments and helpful suggestions. The CCLM is a
757 community model of German climate research (www.clm-community.eu). We
758 acknowledge the German Climate Computing Center (DKRZ) for providing computer
759 hardware for our simulations conducted under a project entitled “Regional

760 Atmospheric Modeling". Publicly accessible datasets used in the study are greatly
761 appreciated. We thank Burkhardt Rockel for his assistance with regional climate
762 modeling. We also thank Zhengyu Han for his help in observation data collecting.
763 Funding for this study was provided through the National Key Research and
764 Development Program of China (2017YFA0604101), from the National Natural Science
765 Foundation of China (41706019), from the Youth Innovation Promotion Association of
766 the Chinese Academy of Sciences (CAS), from the CAS Interdisciplinary Innovation
767 Team, through the Key Research Program of Frontier Sciences of the CAS, from the
768 General Financial Grant (2017M612357) and from the Special Financial Grant
769 (2017T100520) under the China Postdoctoral Science Foundation.

770 **References**

771 Bao JW, Feng JM, Wang YL (2015) Dynamical downscaling simulation and future
772 projection of precipitation over China. *J Geophys Res-Atmospheres* 120:8227–8243.
773 Brown JR, Jakob C, Haynes JM (2010) An evaluation of rainfall frequency and intensity
774 over the Australian region in a global climate model. *Journal of Climate* 23(24):6504-
775 6525.
776 Chen L, Frauenfeld OW (2014) A comprehensive evaluation of precipitation
777 simulations over China based on CMIP5 multimodel ensemble projections: CMIP5
778 PRECIPITATION IN CHINA. *J Geophys Res Atmospheres* 119:5767–5786. doi:
779 10.1002/2013JD021190
780 Christensen JH, Carter TR, Rummukainen M, Amanatidis G. (2007) Evaluating the

781 performance and utility of regional climate models: the prudence project. Climatic
782 Change 81(1): 1-6.

783 Collins WJ, Bellouin N, Doutriaux-Boucher M, et al (2011) Development and evaluation
784 of an Earth-System model – HadGEM2. Geosci Model Dev 4:1051–1075. doi:
785 10.5194/gmd-4-1051-2011

786 Dee DP, Uppala SM, Simmons AJ, et al (2011) The ERA-Interim reanalysis: configuration
787 and performance of the data assimilation system. Q J R Meteorol Soc 137:553–597.
788 doi: 10.1002/qj.828

789 Dosio A, Panitz HJ, Schubert-Frisius M, Luthi D (2015) Dynamical downscaling of CMIP5
790 global circulation models over CORDEX-Africa with COSMO-CLM: evaluation over the
791 present climate and analysis of the added value. Clim Dyn 44:2637–2661.

792 Fekete BM, Vörösmarty CJ, Roads JO, Willmott CJ (2004) Uncertainties in precipitation
793 and their impacts on runoff estimates. Journal of Climate 17(2):294–304.

794 Feng J, Wei T, Dong W, Wu Q, Wang Y (2014) CMIP5/AMIP GCM simulations of East
795 Asian summer monsoon. Advances in Atmospheric Sciences 31(4):836–850.

796 Feser F, Rockel B, von Storch H, et al (2011) Regional Climate Models Add Value to
797 Global Model Data: A Review and Selected Examples. Bull Am Meteorol Soc 92:1181–
798 1192. doi: 10.1175/2011BAMS3061.1

799 Frich P, Alexander LV, Della-Marta PM, Gleason B, Haylock M, Tank AK, Peterson T (2002)
800 Observed coherent changes in climatic extremes during the second half of the
801 twentieth century. Climate Research 19(3):193–212.

802 Fu C, Wang S, Xiong Z, et al (2005) Regional Climate Model Intercomparison Project for

- 803 Asia. Bull Am Meteorol Soc 86:257–266. doi: 10.1175/BAMS-86-2-257
- 804 Gao X, Shi Y, Zhang D, Giorgi F (2012a) Climate change in China in the 21st century as
805 simulated by a high resolution regional climate model. Chinese Science Bulletin
806 57(10):1188-1195.
- 807 Gao X, Shi Y, Zhang D, et al (2012b) Uncertainties in monsoon precipitation projections
808 over china: results from two high-resolution RCM simulations. Climate Research, 52(1),
809 213-226.
- 810 Gao X, Zhao Z, Giorgi F (2002) Changes of extreme events in regional climate
811 simulations over East Asia. Advances in atmospheric sciences 19(5):927-942.
- 812 Gao Y, Chen D (2017) Modeling of Regional Climate over the Tibetan Plateau. Oxford
813 Research Encyclopedia of Climate Science. doi:
814 10.1093/acrefore/9780190228620.013.591
- 815 Giorgetta M, Jungclaus J, Reick C, et al (2012) CMIP5 simulations of the Max Planck
816 Institute for Meteorology (MPI-M) based on the MPI-ESM-LR model: The historical
817 experiment, served by ESGF.
- 818 Giorgi F, Jones C, Asrar GR (2009) Addressing climate information needs at the regional
819 level: the CORDEX framework. World Meteorological Organization (WMO) Bulletin
820 58(3): 175.
- 821 Gelaro R, McCarty W, Suárez MJ, et al (2017) The Modern-Era Retrospective Analysis
822 for Research and Applications, Version 2 (MERRA-2). J Clim 30:5419–5454. doi:
823 10.1175/JCLI-D-16-0758.1
- 824 Giorgi F, Bates GT (1989) The climatological skill of a regional model over complex

- 825 terrain. Mon Weather Rev 117:2325–2347. doi: 10.1175/1520-
- 826 0493(1989)117<2325:TCSOAR>2.0.CO;2
- 827 Giorgi F, Jones C, Asrar GR (2009) Addressing climate information needs at the regional
828 level: the CORDEX framework. Bull - World Meteorol Organ 175–183.
- 829 Guo Y, Dong W, Ren F, et al (2013) Assessment of CMIP5 simulations for China annual
830 average surface temperature and its comparison with CMIP3 simulations. Adv Clim
831 Change Res 9:181–186.
- 832 Harris I, Jones PD, Osborn TJ, Lister DH (2014) Updated high-resolution grids of
833 monthly climatic observations - the CRU TS3.10 Dataset: UPDATED HIGH-RESOLUTION
834 GRIDS OF MONTHLY CLIMATIC OBSERVATIONS. Int J Climatol 34:623–642. doi:
835 10.1002/joc.3711
- 836 Hazeleger W, Severijns C, Semmler T, et al (2010) EC-Earth: A Seamless Earth-System
837 Prediction Approach in Action. Bull Am Meteorol Soc 91:1357–1363. doi:
838 10.1175/2010BAMS2877.1
- 839 Hostetler S, Alder J, Allan A (2011) Dynamically downscaled climate simulations over
840 North America: Methods, evaluation, and supporting documentation for users. US
841 Geological Survey
- 842 Huang B, Polanski S, Cubasch U (2015) Assessment of precipitation climatology in an
843 ensemble of CORDEX-East Asia regional climate simulations. Clim Res 64: 141–158.
844 doi:10.3354/cr01302.
- 845 Huang D-Q, Zhu J, Zhang Y-C, Huang A-N (2013) Uncertainties on the simulated
846 summer precipitation over Eastern China from the CMIP5 models: UNCERTAINTIES ON

- 847 SUMMER PRECIPITATION. J Geophys Res Atmospheres 118:9035–9047. doi:
848 10.1002/jgrd.50695
- 849 Huffman GJ, Adler RF, Morrissey MM, et al (2001) Global Precipitation at One-Degree
850 Daily Resolution from Multisatellite Observations. J Hydrometeorol 2:36–50. doi:
851 10.1175/1525-7541(2001)002<0036:GPAODD>2.0.CO;2
- 852 Huffman GJ, Bolvin DT, Nelkin EJ, et al (2007) The TRMM multisatellite precipitation
853 analysis (TMPA): Quasi-global, multiyear, combined-sensor precipitation estimates at
854 fine scales. J Hydrometeorol 8(1):38–55.
- 855 IPCC (2014) Climate Change 2014–Impacts, Adaptation and Vulnerability. Cambridge
856 University Press, Cambridge, United Kingdom and New York, NY, USA
- 857 Jacob D, Petersen J, Eggert B, et al (2014) Euro-cordex: new high-resolution climate
858 change projections for european impact research. Regional Environmental Change
859 14(2): 579-581
- 860 Ji Z, Kang S (2015) Evaluation of extreme climate events using a regional climate model
861 for China. International Journal of Climatology 35(6):888-902.
- 862 Kessler E (1969) On the Distribution and Continuity of Water Substance in Atmospheric
863 Circulations. In: On the Distribution and Continuity of Water Substance in Atmospheric
864 Circulations. American Meteorological Society, Boston, MA, pp 1–84
- 865 Kobayashi S, Ota Y, Harada Y, et al (2015) The JRA-55 Reanalysis: General Specifications
866 and Basic Characteristics. J Meteorol Soc Jpn Ser II 93:5–48 . doi: 10.2151/jmsj.2015-
867 001
- 868 Kumar P, Kotlarski S, Moseley C, et al (2015) Response of Karakoram - Himalayan

- 869 glaciers to climate variability and climatic change: A regional climate model
870 assessment. *Geophysical Research Letters* 42(6):1818-1825.
- 871 Kusunoki S, Mizuta R, Matsueda M (2011) Future changes in the East Asian rain band
872 projected by global atmospheric models with 20-km and 60-km grid size. *Clim Dyn*
873 37:2481–2493.
- 874 Lee J-W, Hong S-Y (2014) Potential for added value to downscaled climate extremes
875 over Korea by increased resolution of a regional climate model. *Theoretical and*
876 *applied climatology* 117(3-4):667-677.
- 877 Lee J-W, Hong S-Y, Chang E-C, et al (2014) Assessment of future climate change over
878 East Asia due to the RCP scenarios downscaled by GRIMs-RMP. *Clim Dyn* 42:733–747.
879 doi: 10.1007/s00382-013-1841-6
- 880 Li D (2017) Added value of high-resolution regional climate model: selected cases over
881 the Bohai Sea and the Yellow Sea areas: ADDED VALUE OF HIGH-RESOLUTION
882 REGIONAL CLIMATE MODEL. *Int J Climatol* 37:169–179. doi: 10.1002/joc.4695
- 883 Li D, von Storch H, Geyer B (2016) High-resolution wind hindcast over the Bohai Sea
884 and the Yellow Sea in East Asia: Evaluation and wind climatology analysis: Wind
885 Hindcast Evaluation and Climatology. *J Geophys Res Atmospheres* 121:111–129. doi:
886 10.1002/2015JD024177
- 887 Liu Y, Giorgi F, Washington WM (1994) Simulation of summer monsoon climate over
888 East Asia with an NCAR regional climate model. *Monthly Weather Review*
889 122(10):2331-2348.
- 890 Lott F, Miller MJ (1997) A new subgrid-scale orographic drag parametrization: Its

- 891 formulation and testing. Q J R Meteorol Soc 123:101–127. doi:
892 10.1002/qj.49712353704
- 893 McSweeney CF, Jones RG, Lee RW, Rowell DP (2015) Selecting CMIP5 GCMs for
894 downscaling over multiple regions. Clim Dyn 44:3237–3260.
- 895 Mehran A, AghaKouchak A, Phillips TJ (2014) Evaluation of CMIP5 continental
896 precipitation simulations relative to satellite - based gauge - adjusted observations. J
897 Geophys Res Atmospheres 119:1695 – 1707.
- 898 Moss RH, Edmonds JA, Hibbard KA, et al (2010) The next generation of scenarios for
899 climate change research and assessment. Nature 463:747–756. doi:
900 10.1038/nature08823
- 901 Niu X, Wang S, Tang J, et al (2015) Multimodel ensemble projection of precipitation in
902 eastern China under A1B emission scenario. J Geophys Res Atmospheres 120:9965–
903 9980.
- 904 Oh S-G, Park J-H, Lee S-H, Suh M-S (2014) Assessment of the RegCM4 over East Asia
905 and future precipitation change adapted to the RCP scenarios: ASSESSMENT OF THE
906 REGCM4 OVER EAST ASIA. J Geophys Res Atmospheres 119:2913–2927. doi:
907 10.1002/2013JD020693
- 908 Park C, Min SK, Lee D, et al (2016) Evaluation of multiple regional climate models for
909 summer climate extremes over East Asia. Clim Dyn 46:2469–2486.
- 910 Ritter B, Geleyn J-F (1992) A Comprehensive Radiation Scheme for Numerical Weather
911 Prediction Models with Potential Applications in Climate Simulations. Mon Weather
912 Rev 120:303–325. doi: 10.1175/1520-0493(1992)120<0303:ACRSFN>2.0.CO;2

- 913 Rockel B, Geyer B (2008) The performance of the regional climate model CLM in
914 different climate regions, based on the example of precipitation. Meteorol Z 17:487–
915 498.
- 916 Rockel B, Roads J, Meinke I, et al (2005) ICTS (Inter-CSE Transferability Study): an
917 application of CEOP data. In Preprints, 16th Conf. on Climate Variability and Change,
918 San Diego, CA, Amer. Meteor. Soc., CD-ROM (Vol. 7).
- 919 Rockel B, Will A, Hense A (2008) The Regional Climate Model COSMO-CLM (CCLM).
920 Meteorol Z 17:347–348. doi: 10.1127/0941-2948/2008/0309
- 921 Schättler U, Doms G, Schraff C (2008) A description of the nonhydrostatic regional
922 COSMO-model part VII: user's guide. Dtsch Wetterd Rep COSMO-Model 4:142.
- 923 Schneider U, Becker A, Finger P, et al (2014) GPCC's new land surface precipitation
924 climatology based on quality-controlled in situ data and its role in quantifying the
925 global water cycle. Theor Appl Climatol 115:15–40. doi: 10.1007/s00704-013-0860-x
- 926 Schrödin R, Heise E (2002) A new multi-layer soil-model. COSMO Newsl 2: 139–151.
- 927 Schulz J-P (2008) Introducing sub-grid scale orographic effects in the COSMO model.
928 COSMO Newsl 9:29–36.
- 929 Sillmann J, Kharin VV, Zhang X, et al (2013) Climate extremes indices in the CMIP5
930 multimodel ensemble: Part 1. Model evaluation in the present climate. J Geophys Res-
931 Atmospheres 118:1716–1733.
- 932 Song F, Zhou T (2014) Interannual variability of East Asian summer monsoon simulated
933 by CMIP3 and CMIP5 AGCMs: Skill dependence on Indian Ocean–western Pacific
934 anticyclone teleconnection. Journal of Climate 27(4):1679–1697.

- 935 Sperber KR, Annamalai H, Kang I-S, et al (2013) The Asian summer monsoon: an
936 intercomparison of CMIP5 vs. CMIP3 simulations of the late 20th century. *Clim Dyn*
937 41:2711–2744.
- 938 Tang J, Li Q, Wang S, et al (2016) Building Asian climate change scenario by multi -
939 regional climate models ensemble. Part I: surface air temperature. *Int J Climatol*
940 36:4241 – 4252.
- 941 Tiedtke M (1989) A Comprehensive Mass Flux Scheme for Cumulus Parameterization
942 in Large-Scale Models. *Mon Weather Rev* 117:1779–1800. doi: 10.1175/1520-
943 0493(1989)117<1779:ACMFSF>2.0.CO;2
- 944 Um M-J, Kim Y, Kim J (2017) Evaluating historical drought characteristics simulated in
945 CORDEX East Asia against observations.
- 946 Van der Linden P, Mitchell JE (2009) ENSEMBLES: Climate change and its impacts-
947 Summary of research and results from the ENSEMBLES project. Met Office Hadley
948 Centre, FitzRoy Road, Exeter EX1 3PB, UK.
- 949 Volodire A, Sanchez-Gomez E, Salas y Méria D, et al (2013) The CNRM-CM5.1 global
950 climate model: description and basic evaluation. *Clim Dyn* 40:2091–2121. doi:
951 10.1007/s00382-011-1259-y
- 952 von Storch H, Feser F, Geyer B, et al (2017) Regional reanalysis without local data:
953 Exploiting the downscaling paradigm. *J Geophys Res Atmospheres* 122:8631–8649. doi:
954 10.1002/2016JD026332
- 955 von Storch H, Zwiers FW (1999) Statistical analysis in climate research. Cambridge
956 University Press, Cambridge, UK

- 957 Wang B, Bao Q, Hoskins B, et al (2008) Tibetan Plateau warming and precipitation
958 changes in East Asia. *Geophys Res Lett.* doi: 10.1029/2008GL034330
- 959 Wang D, Menz C, Simon T, et al (2013) Regional dynamical downscaling with CCLM
960 over East Asia. *Meteorol Atmospheric Phys* 121:39–53.
- 961 WCRP, 2009: Coordinated Regional Climate Downscaling Experiment (CORDEX).
- 962 Accessed 25 March 2018,
963 http://cordex.org/?option=com_content&view=featured&Itemid=476.
- 964 Wu FT, Wang SY, Fu CB, et al (2016) Evaluation and projection of summer extreme
965 precipitation over East Asia in the Regional Model Inter-comparison Project. *Clim Res*
966 69:45–58.
- 967 Xie P, Chen M, Yang S, Yatagai A, Hayasaka T, Fukushima Y, Liu C (2007) A gauge-based
968 analysis of daily precipitation over East Asia. *Journal of Hydrometeorology* 8(3):607–
969 26.
- 970 Xie ZH, Zeng YJ, Xia J, et al (2017) Coupled modeling of land hydrology–regional climate
971 including human carbon emission and water exploitation. *Advances in Climate Change*
972 Research 8(2):68–79.
- 973 Yang K, Koike T, Ye B, Bastidas L (2005) Inverse analysis of the role of soil vertical
974 heterogeneity in controlling surface soil state and energy partition. *Journal of*
975 *Geophysical Research: Atmospheres*: 110(D8).
- 976 Yatagai A, Kamiguchi K, Arakawa O, et al (2012) APHRODITE: Constructing a Long-Term
977 Daily Gridded Precipitation Dataset for Asia Based on a Dense Network of Rain Gauges.
978 *Bull Am Meteorol Soc* 93:1401–1415 . doi: 10.1175/BAMS-D-11-00122.1

- 979 Zhang D, Zakey AS, Gao X, Giorgi F, Solmon F (2009) Simulation of dust aerosol and its
 980 regional feedbacks over East Asia using a regional climate model. *Atmospheric*
 981 *Chemistry and Physics* 9(4):1095-1110.
- 982 Zhang X, Alexander L, Hegerl GC, Jones P, Tank AK, Peterson TC, Trewin B, Zwiers FW
 983 (2011) Indices for monitoring changes in extremes based on daily temperature and
 984 precipitation data. *Wiley Interdisciplinary Reviews: Climate Change* 2(6):851-870.
- 985 Zhou T, Yu R (2005) Atmospheric water vapor transport associated with typical
 986 anomalous summer rainfall patterns in China. *J Geophys Res.* doi:
 987 10.1029/2004JD005413
- 988 Zhou WD, Tang JP, Wang XY, et al (2016) Evaluation of regional climate simulations over
 989 the CORDEX-EA-II domain using the COSMO-CLM model. *Asia-Pac J Atmospheric Sci*
 990 52:107–127.
- 991 Zou LW, Zhou TJ (2013) Near future (2016-40) summer precipitation changes over
 992 China as projected by a regional climate model (RCM) under the RCP8.5 emissions
 993 scenario: Comparison between RCM downscaling and the driving GCM. *Adv*
 994 *Atmospheric Sci* 30:806–818.
- 995 Zou LW, Zhou TJ, Peng DD (2016) Dynamical downscaling of historical climate over
 996 CORDEX East Asia domain: A comparison of regional ocean-atmosphere coupled
 997 model to stand-alone RCM simulations. *J Geophys Res-Atmospheres* 121:1442–1458.

Table 1. Information on the four GCMs used in the present analysis.

Model	Institution/Country	Grids	Vertical Levels
-------	---------------------	-------	-----------------

CNRM-CM5	National Centre for Meteorological Research, France	256 x 128	31
EC-Earth	EC-EARTH consortium, Europe	320 x 160	62
HadGEM2(-ES)	Met Office Hadley Centre, UK	360 x 181	38
MPI-ESM-LR	Max Planck Institute for Meteorology, Germany	192 x 96	47

998 Table 2. Basic configuration schemes and invariant external forcings of the CCLM
 999 simulations

Physical parameterization scheme		Invariant external forcings	
Convection scheme	Tiedtke (1989)	Orography	GLOBE (NOAA/NGDC)
Time-integration scheme	Runge-Kutta scheme	Surface roughness	GLOBE (NOAA/NGDC), GLC2000 (JRC Ispra)
Turbulence Scheme	Prognostic turbulent kinetic energy closure scheme	Land-sea fraction, parameters of vegetation, leaf area, and root depth	GLC2000 (JRC Ispra)
Radiation scheme	Ritter and Geleyn (1992)	Near surface temperature	CRU (University of East Anglia)
Microphysics scheme	Kessler-type scheme Kessler (1969)	Soil type	Digital Soil Map of the World (Food and Agriculture Organization of the United Nations)
Land surface processes	multi-layer soil model TERRA_ML (Schrodin and Heise 2002)	Surface albedo	MODIS soil color derived soil albedo (NASA)
Subgrid-scale orography scheme	Lott and Miller 1997; Schulz 2008	Aerosol optical thickness	NASA/GISS (Global Aerosol Climatology Project)

1000 Table 3. Reference datasets for model evaluation

1001

Physical parameterization scheme		Invariant external forcings	
Convection scheme	Tiedtke (1989)	Orography	GLOBE (NOAA/NGDC)
Time-integration scheme	Runge-Kutta scheme	Surface roughness	GLOBE (NOAA/NGDC), GLC2000 (JRC Ispra)
Turbulence Scheme	Prognostic turbulent kinetic energy closure scheme	Land-sea fraction, parameters of vegetation, leaf area, and root depth	GLC2000 (JRC Ispra)
Radiation scheme	Ritter and Geleyn (1992)	Near surface temperature	CRU (University of East Anglia)
Microphysics scheme	Kessler-type scheme Kessler (1969)	Soil type	Digital Soil Map of the World (Food and Agriculture Organization of the United Nations)
Land surface processes	multi-layer soil model TERRA_ML (Schrodin and Heise 2002)	Surface albedo	MODIS soil color derived soil albedo (NASA)
Subgrid-scale orography scheme	Lott and Miller 1997; Schulz 2008	Aerosol optical thickness	NASA/GISS (Global Aerosol Climatology Project)

1002 **Figure Captions:**

1003 Fig. 1 Model domain and orography of the CORDEX-EA simulations. The six sub-regions
 1004 are western China (WC), Mongolia (MG), southern China (SC), northern China (NC),
 1005 northeastern China (NE), and the Korean Peninsula and Japan (KJ).

1006 Fig. 2 (a) Observed seasonal mean temperature (°C) of the CRU for DJF for 1979/12-
1007 2005/11, (b-d) Biases of the other reanalysis datasets against the CRU, (e-i and j-n)
1008 Biases of the GCMs, CCLM simulations and ensemble means against the CRU, and (o-
1009 s) added value index of seasonal mean temperatures for each GCM-CCLM combination.

1010 Fig. 3 The same as those shown in Fig. 2 but for the JJA.

1011 Fig. 4 Heatmaps showing statistical metrics of (a, b) regional means of bias, (c, d)
1012 spatial correlations and (e, f) STDE between GCM/CCLM/reanalysis datasets and CRU
1013 surface temperature derived from the DJF (left column) and JJA (right column) for
1014 different sub-regions. ‘Land’ denotes the mean for all land areas in the domain.

1015 Fig. 5 (a) Observed seasonal mean rainfall (in mm/day) derived from the GPCP for the
1016 DJF for 1996/12-2005/11, (b-e) Biases of the TRMM (1998/12-2005/11), GPCC, CRU
1017 and APHRO (1996/12-2005/11) against the GPCP respectively (f-j and k-o), Biases of
1018 the GCMs and CCLM simulations and corresponding ensemble means against the
1019 GPCP respectively (p-t), and added value index of seasonal mean rainfall for each GCM-
1020 CCLM combination. Note: the GPCC, CRU and APHRO datasets only cover land areas.

1021 Fig. 6 The same as those shown in Fig. 5 but for the JJA.

1022 Fig. 7 The same as those shown in Fig. 4 but for precipitation with GPCC precipitation
1023 used as the reference dataset.

1024 Fig. 8 Mean annual cycle of rainfall (in mm/day) derived from observations (GPCP,
1025 GPCC, CRU, APHRO and TRMM), GCMs and CCLM simulations for 6 sub-regions and
1026 the land area of the CORDEX-EA domain (the period covers 1979/12-2005/11 except
1027 for the GPCP (1996/12-2005/11) and TRMM (1998/12-2005/11)).

1028 Fig. 9 Box and whisker plots for the 6 sub-regions and the land area of the domain for
1029 the rainfall distribution of the DJF. The base and top of the box denote the 25th and
1030 75th percentiles, respectively; the band within the box is the median; ends of the
1031 whiskers represent minimum and maximum values; and the black circle and black
1032 point denote 5th and 95th percentiles, respectively. Note differences shown in the y-
1033 axis. (The period covers the DJF of 1996/12-2005/11 except for TRMM (the DJF of
1034 1998/06-2005/11)).

1035 Fig. 10 The same as those shown in Fig. 9 but for the JJA.

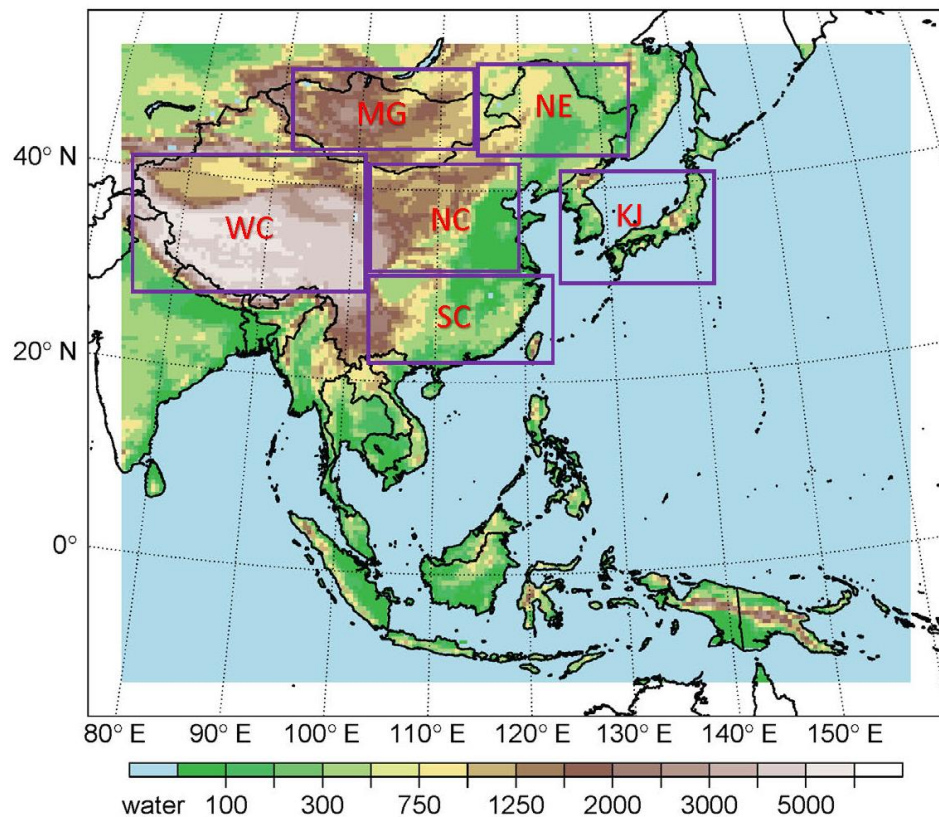
1036 Fig. 11 (a) Winter (DJF) mean water vapor mixing ratio (shading, g/kg) and wind vectors
1037 (arrows, m/s) for the ERAI reanalysis (b-e) biases of four CCLM simulations relative to
1038 (a). (f-i) Biases in the water vapor transport (shading and arrows, $\text{ms}^{-1}\text{gkg}^{-1}$) of CCLM
1039 simulations against ERAI reanalysis data for 1996/12 –2005/11 at 850 hPa pressure
1040 level.

1041 Fig. 12 The same as those shown in Fig. 11 but for the JJA.

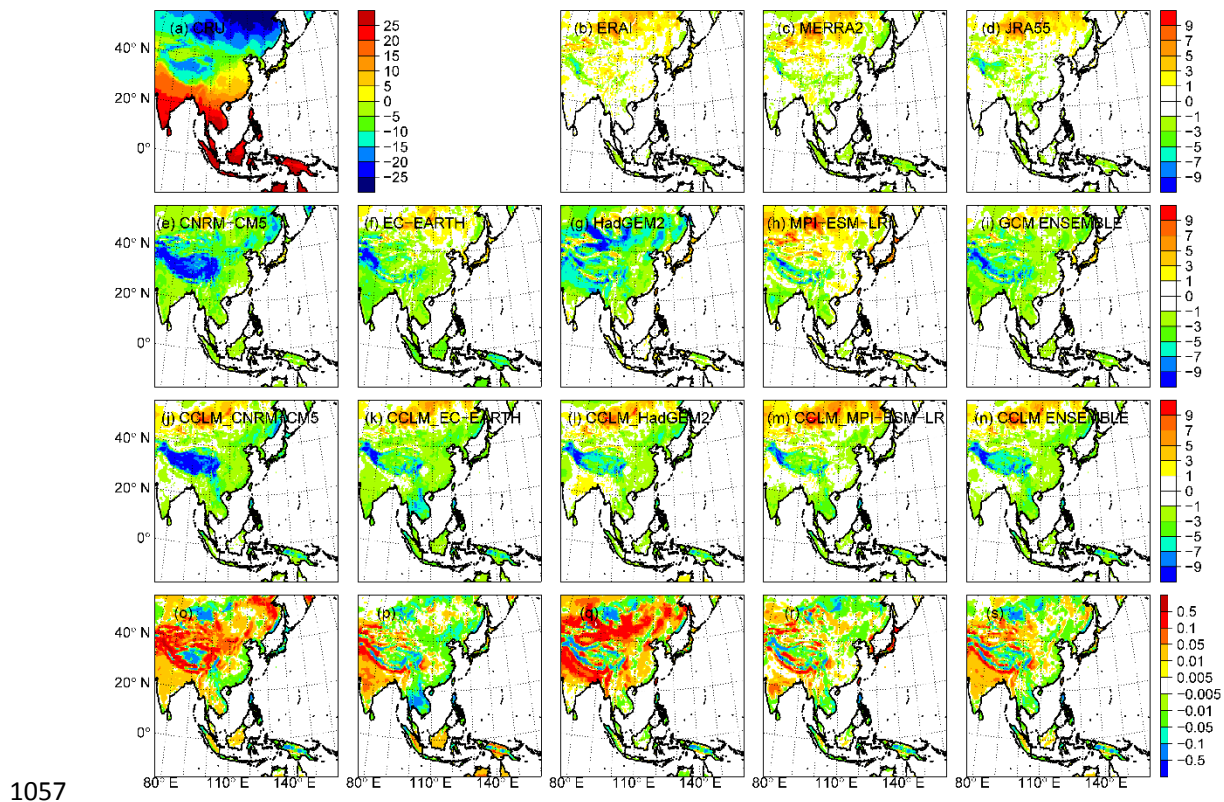
1042 Fig. 13 (a) Mean precipitation amount (mm) for wet days with precipitation levels of
1043 ≥ 1.0 mm (Simple daily intensity index, SDII index) for GPCP for 1996/12-2005/11, (b-f
1044 and g-k) Biases (mm) of GCMs and CCLM simulations and their ensemble means
1045 relative to the GPCP, (l-p) added value index for the SDII for each GCM-CCLM
1046 combination.

1047 Fig. 14 The same as those shown in Fig. 13 but for the maximum number of
1048 consecutive days with precipitation levels of < 1.0 mm (Consecutive Dry Days, CDD
1049 index, unit: days).

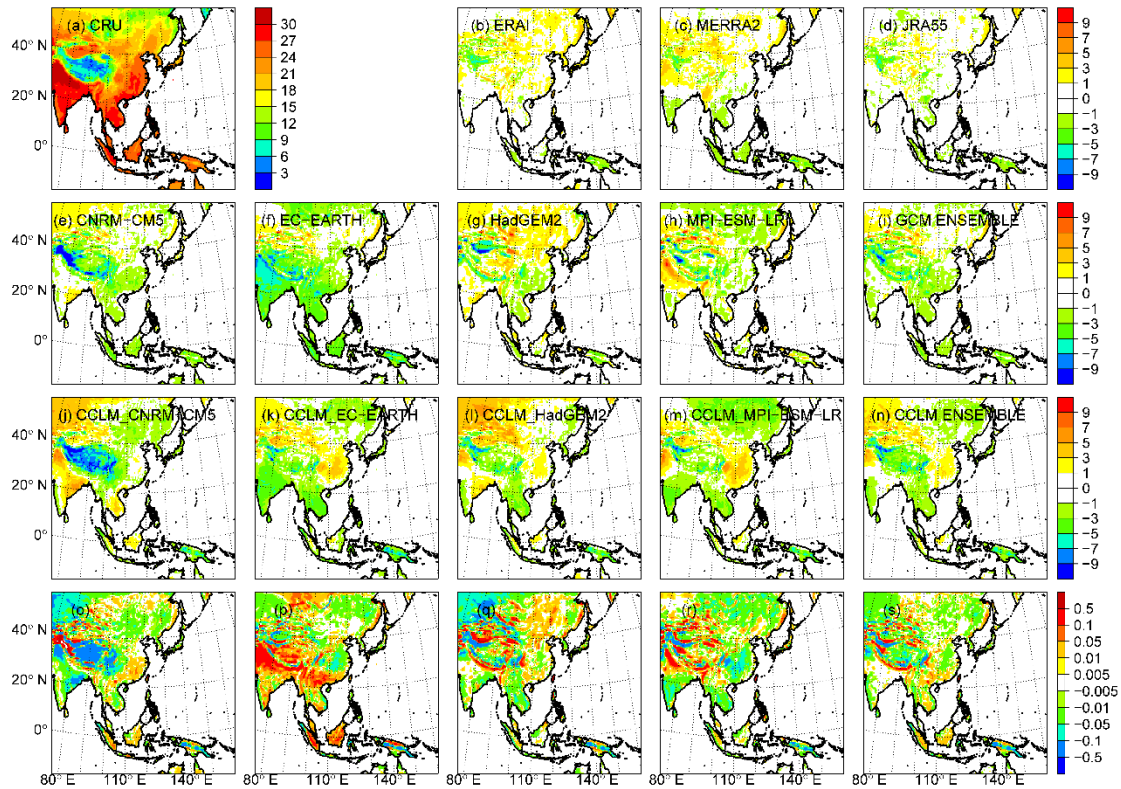
1050 Fig. 15 The same as those shown in Fig. 13 but for the maximum number of
1051 consecutive days with precipitation levels of ≥ 1.0 mm (consecutive wet days, CWD
1052 index, unit: days).



1053
1054 Fig. 1 Model domain and orography of the CORDEX-EA simulations. The six sub-regions
1055 are western China (WC), Mongolia (MG), southern China (SC), northern China (NC),
1056 northeastern China (NE), and the Korean Peninsula and Japan (KJ).

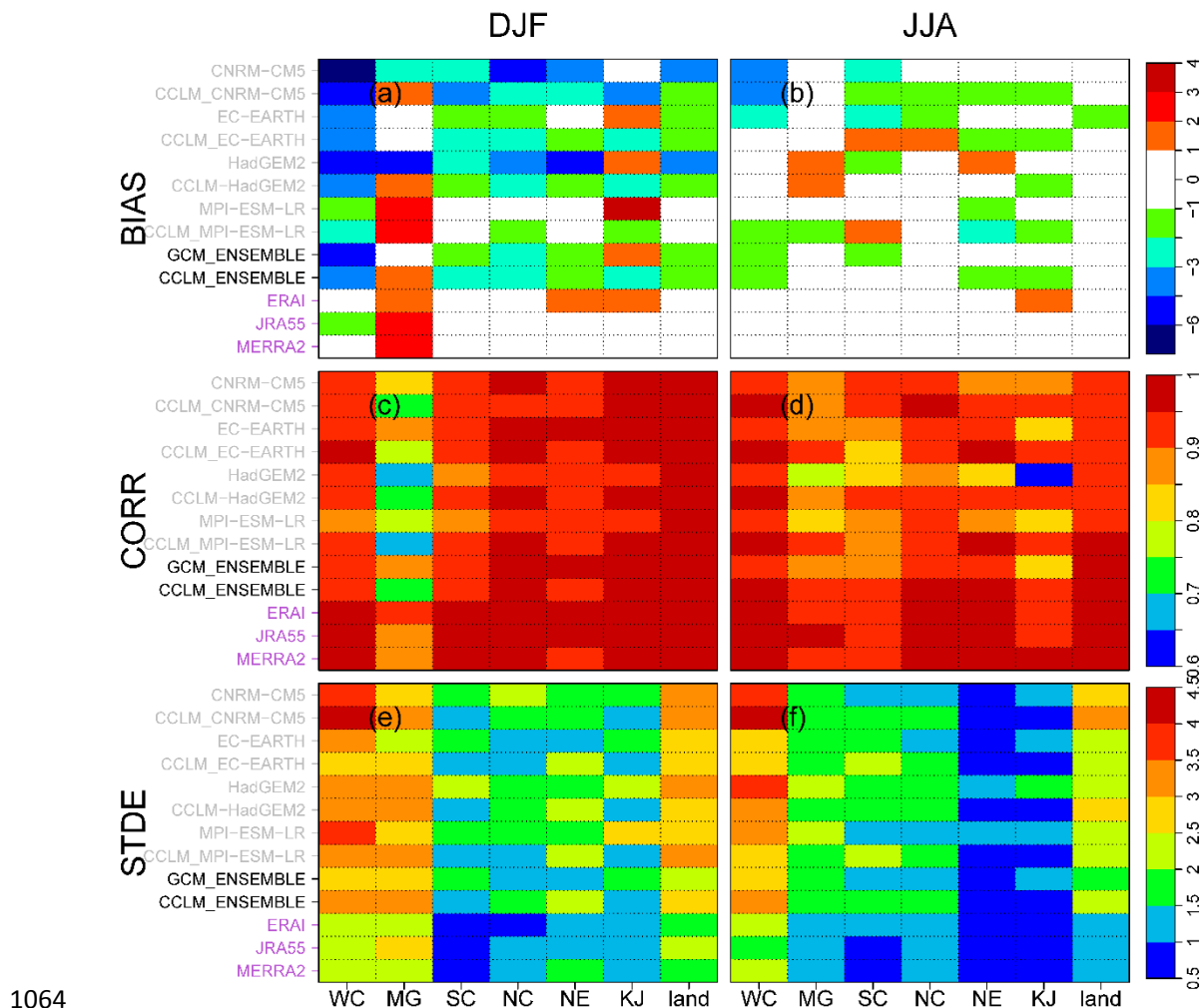


1058 Fig. 2 (a) Observed seasonal mean temperature ($^{\circ}\text{C}$) of the CRU for DJF for 1979/12-
 1059 2005/11, (b-d) Biases of the other reanalysis datasets against the CRU, (e-i and j-n)
 1060 Biases of the GCMs, CCLM simulations and ensemble means against the CRU, and (o-
 1061 s) added value index of seasonal mean temperatures for each GCM-CCLM combination.

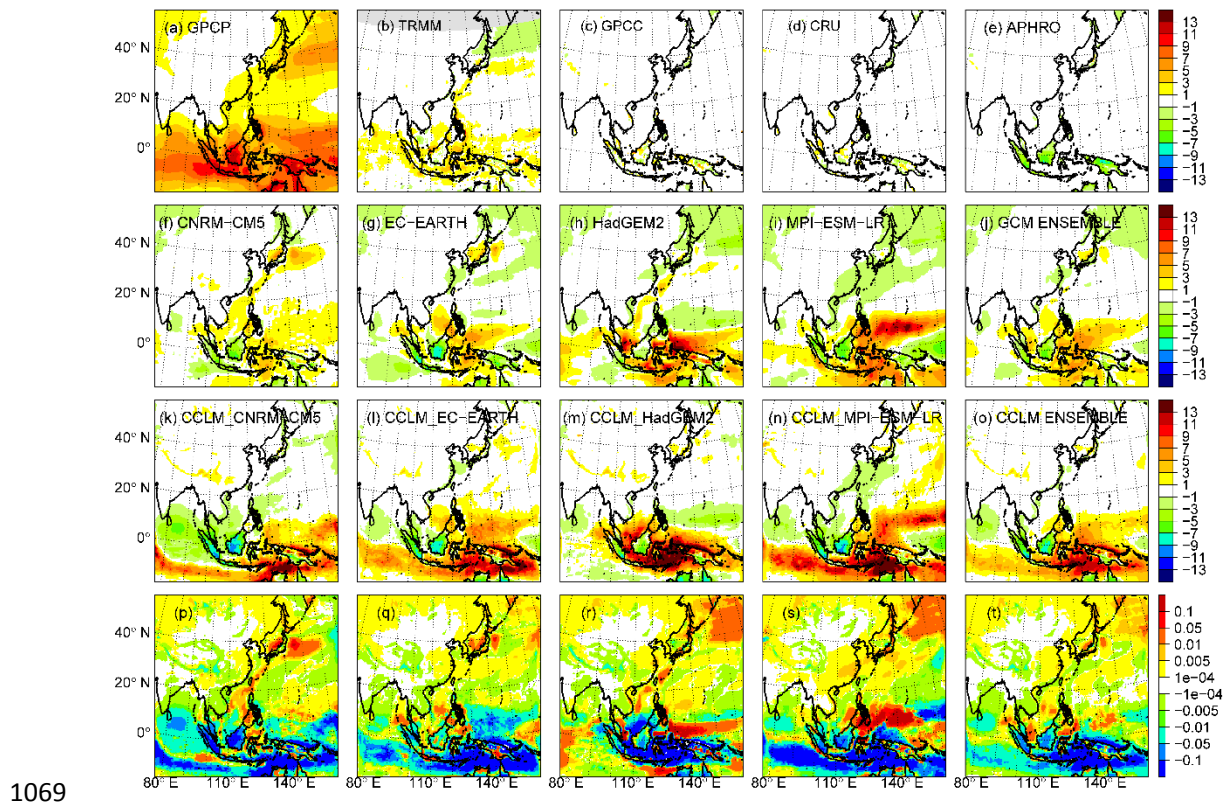


1062

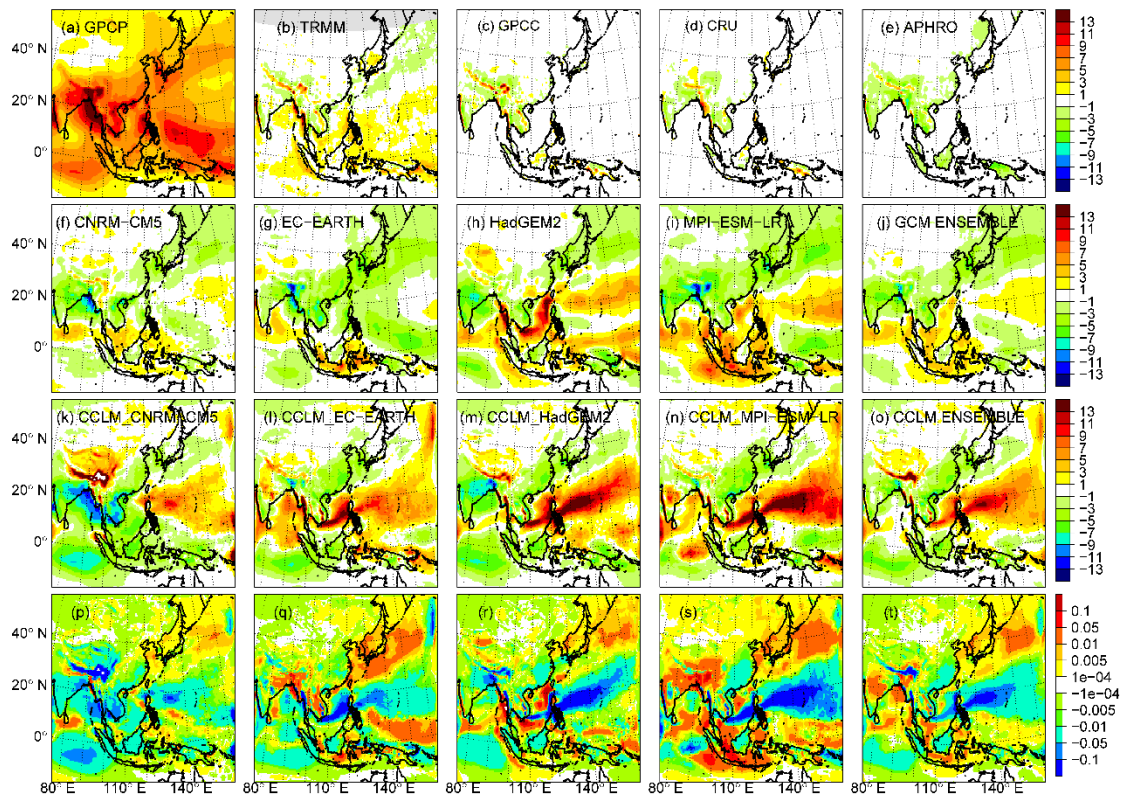
1063 Fig. 3 The same as those shown in Fig. 2 but for the JJA.



1064 Fig. 4 Heatmaps showing statistical metrics of (a, b) regional means of bias, (c, d)
 1065 spatial correlations and (e, f) STDE between GCM/CCLM/reanalysis datasets and CRU
 1066 surface temperature derived from the DJF (left column) and JJA (right column) for
 1067 different sub-regions. ‘Land’ denotes the mean for all land areas in the domain.
 1068

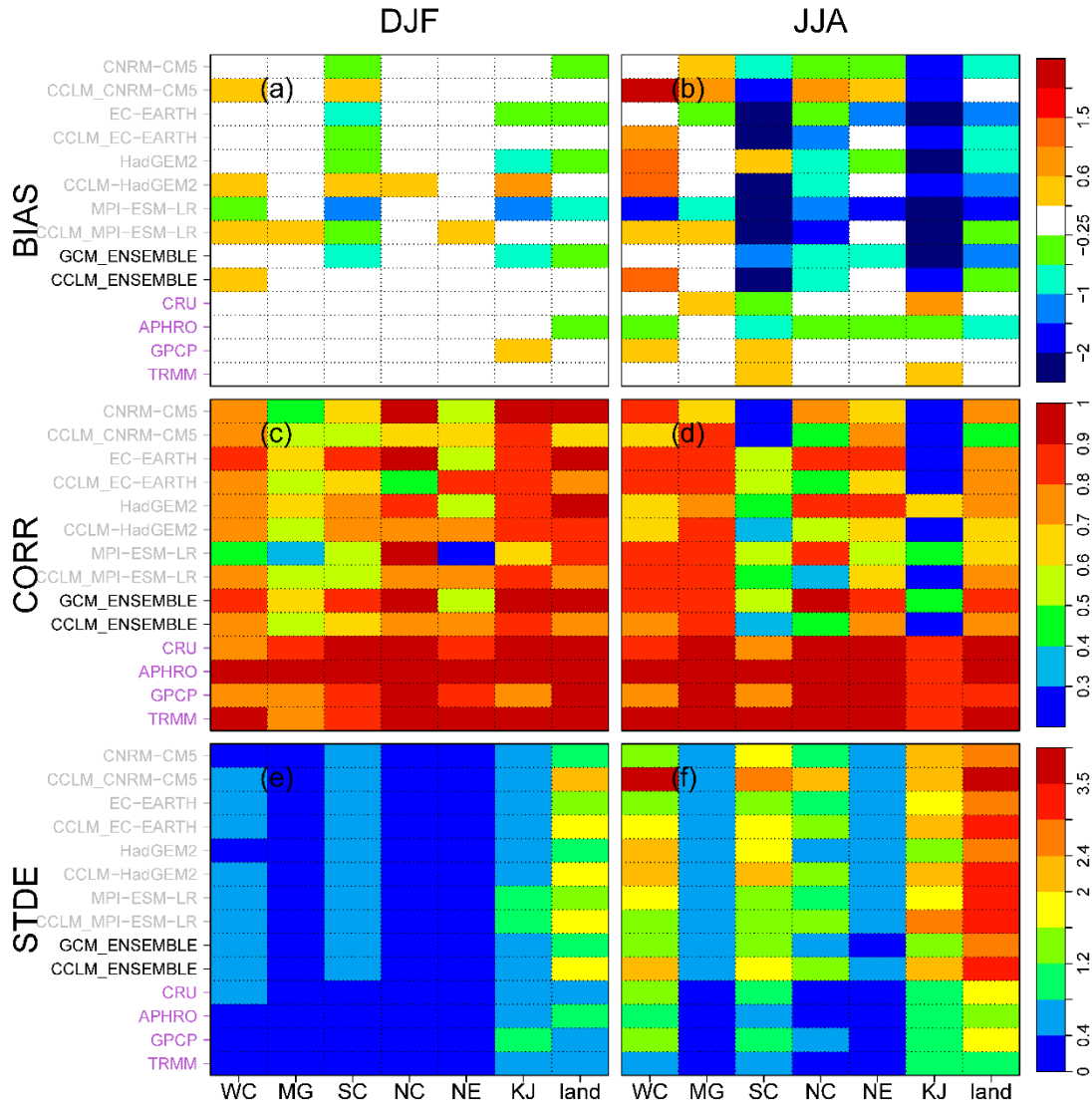


1070 Fig. 5 (a) Observed seasonal mean rainfall (in mm/day) derived from the GPCP for the
 1071 DJF for 1996/12-2005/11, (b-e) Biases of the TRMM (1998/12-2005/11), GPCC, CRU
 1072 and APHRO (1996/12-2005/11) against the GPCP respectively (f-j and k-o), Biases of
 1073 the GCMs and CCLM simulations and corresponding ensemble means against the
 1074 GPCP respectively (p-t), and added value index of seasonal mean rainfall for each GCM-
 1075 CCLM combination. Note: the GPCC, CRU and APHRO datasets only cover land areas.



1076

1077 Fig. 6 The same as those shown in Fig. 5 but for the JJA.

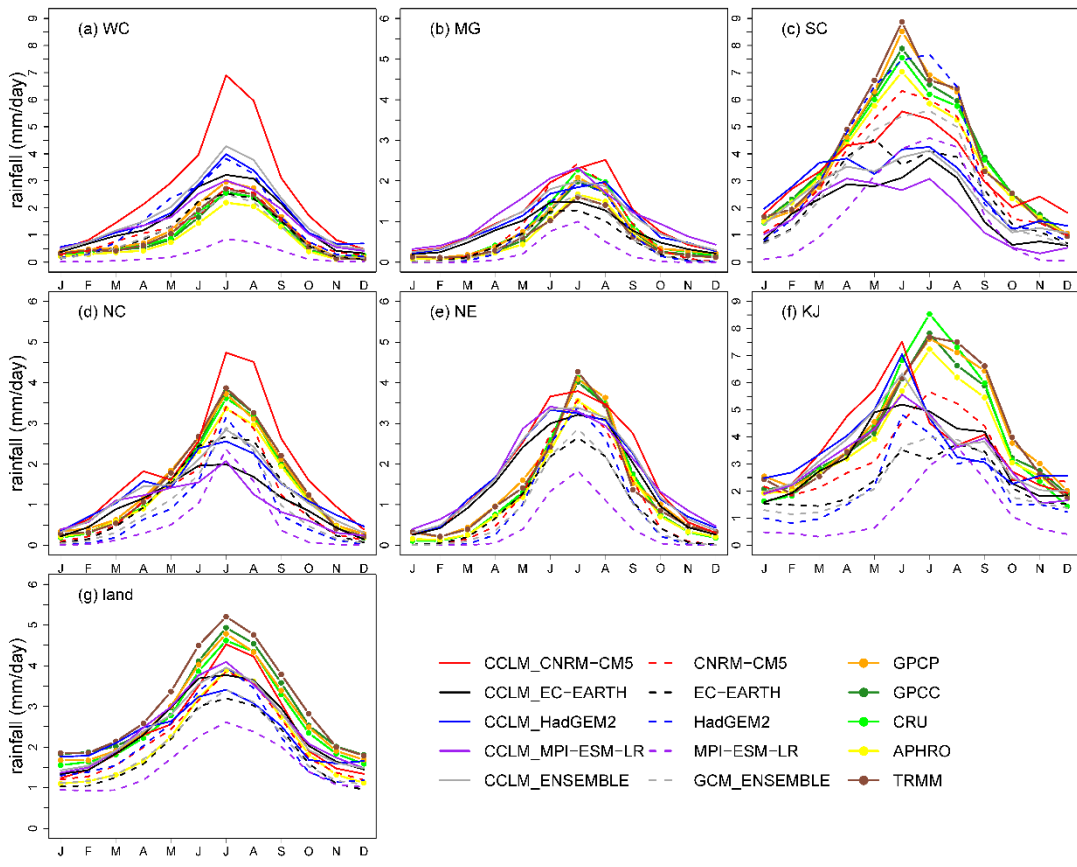


1078

1079 Fig. 7 The same as those shown in Fig. 4 but for precipitation with GPCC precipitation

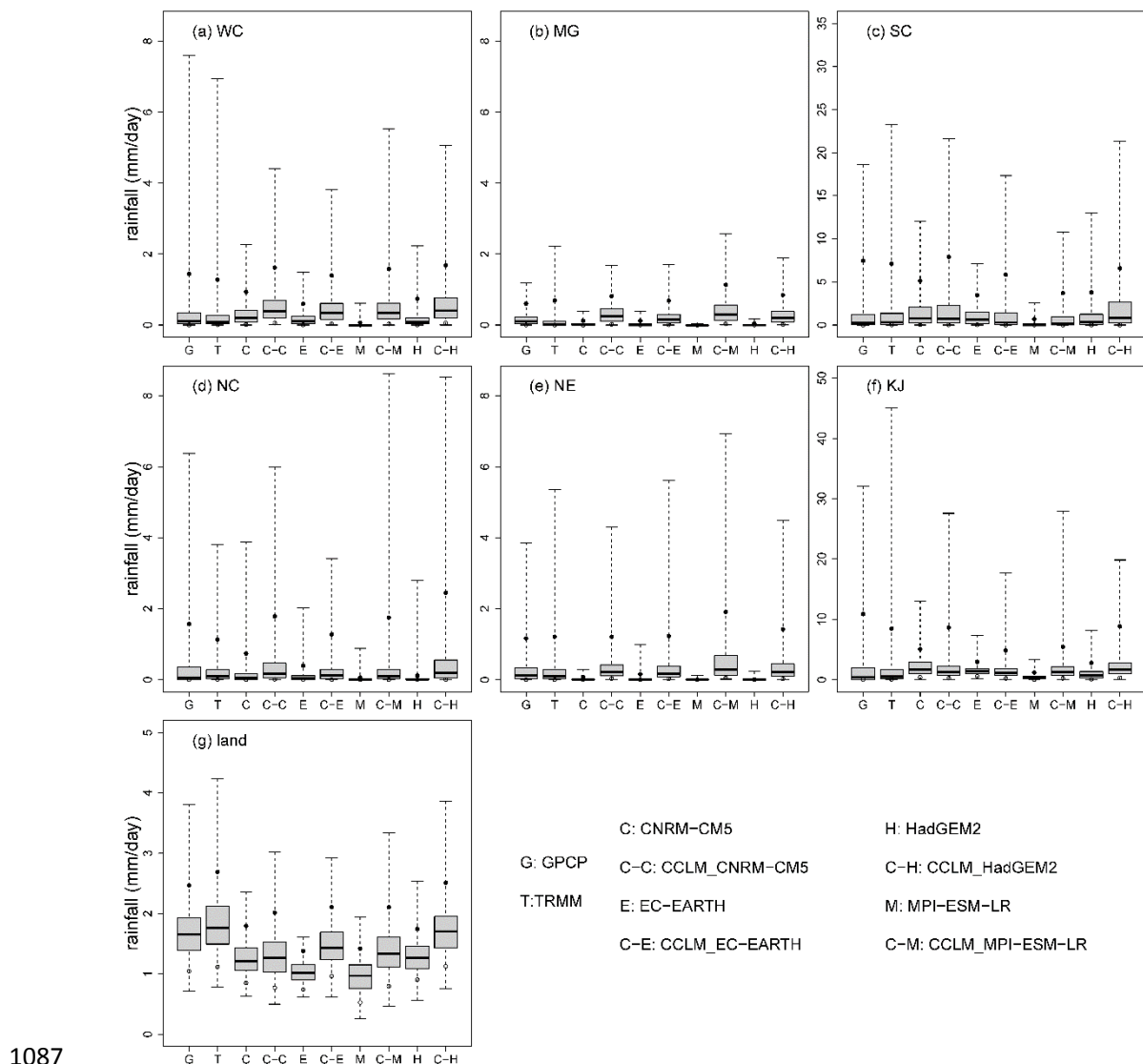
1080 used as the reference dataset.

1081



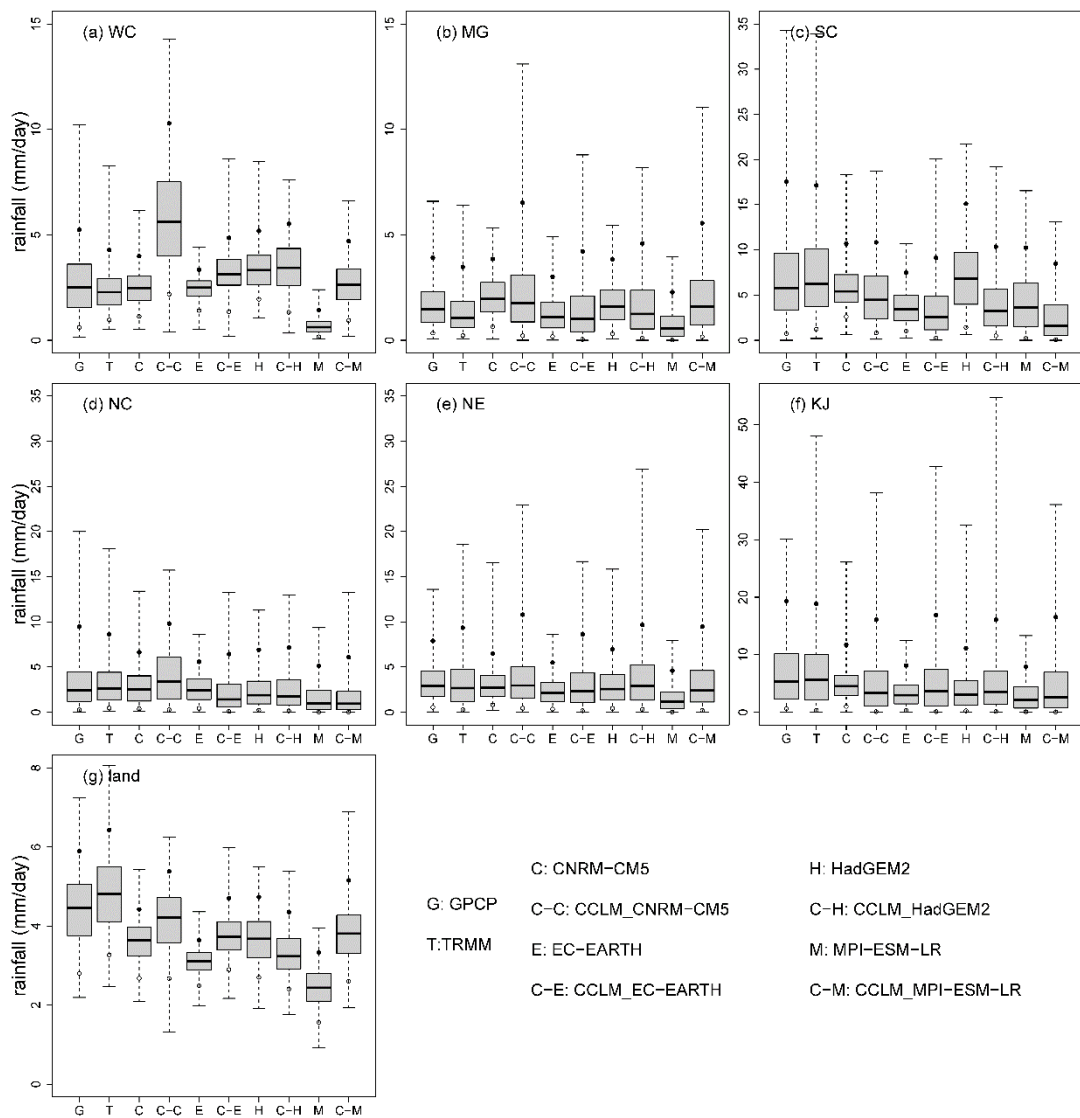
1082

1083 Fig. 8 Mean annual cycle of rainfall (in mm/day) derived from observations (GPCP,
1084 GPCC, CRU, APHRO and TRMM), GCMs and CCLM simulations for 6 sub-regions and
1085 the land area of the CORDEX-EA domain (the period covers 1979/12-2005/11 except
1086 for the GPCP (1996/12-2005/11) and TRMM (1998/12-2005/11)).



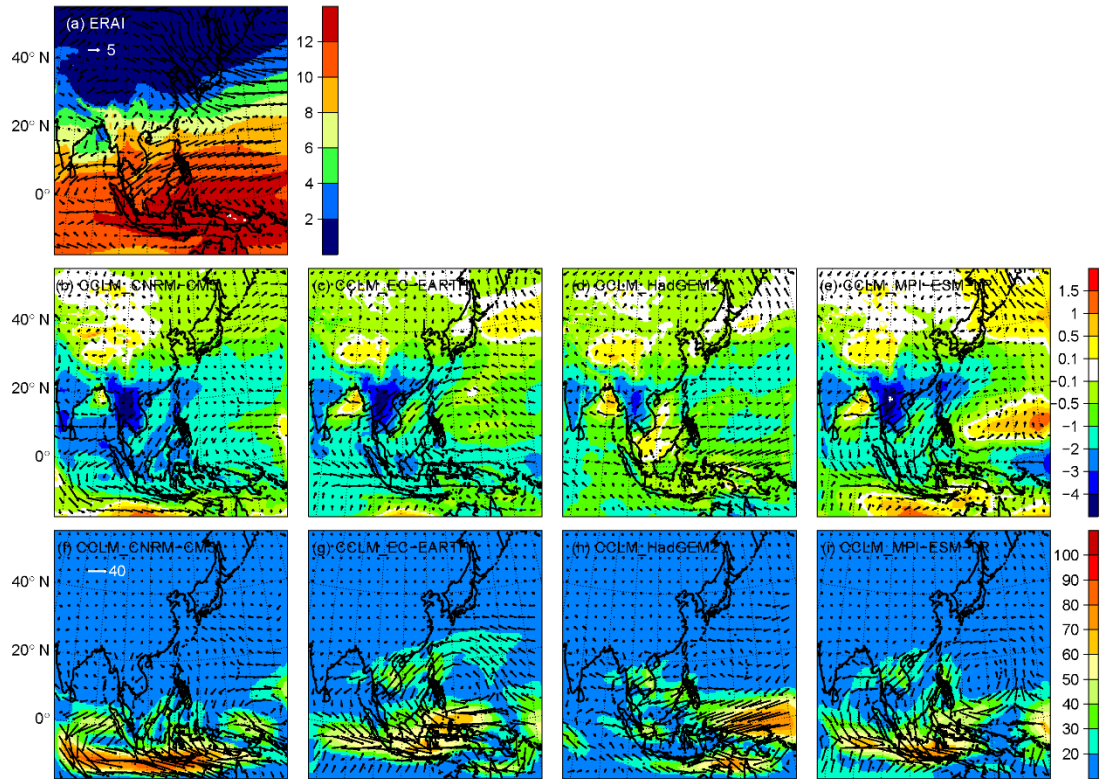
1087

1088 Fig. 9 Box and whisker plots for the 6 sub-regions and the land area of the domain for
 1089 the rainfall distribution of the DJF. The base and top of the box denote the 25th and
 1090 75th percentiles, respectively; the band within the box is the median; ends of the
 1091 whiskers represent minimum and maximum values; and the black circle and black
 1092 point denote 5th and 95th percentiles, respectively. Note differences shown in the y-
 1093 axis. (The period covers the DJF of 1996/12-2005/11 except for TRMM (the DJF of
 1094 1998/06-2005/11)).



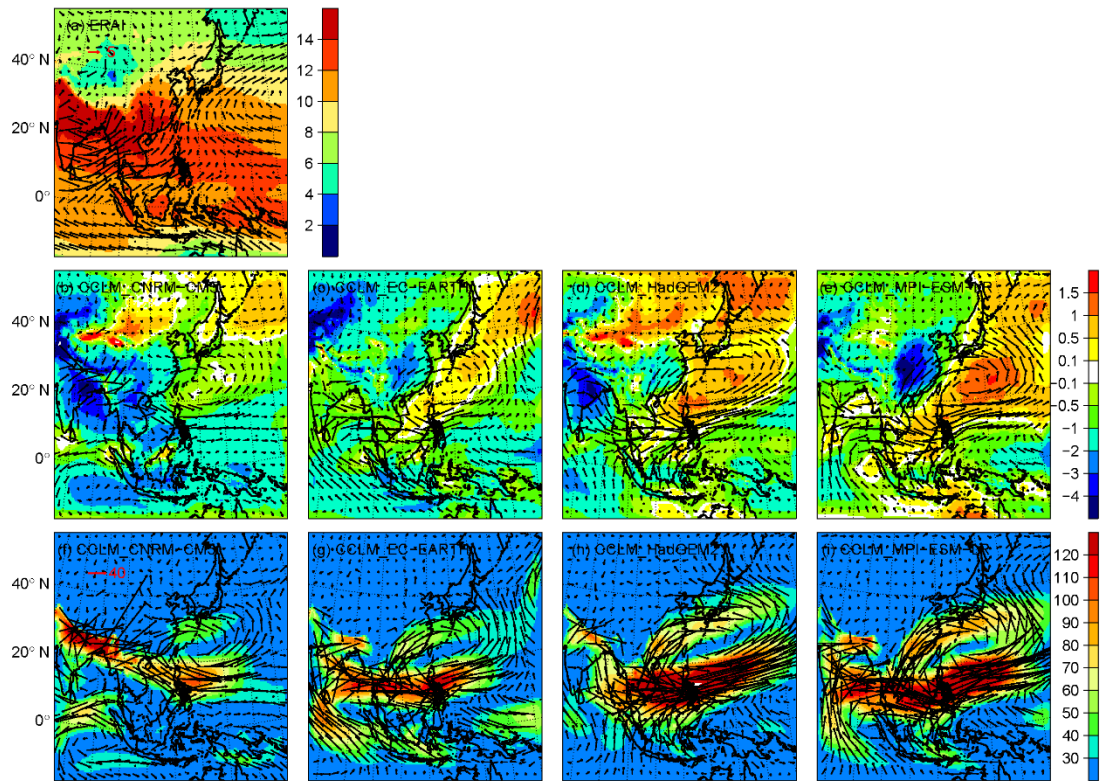
1095

Fig. 10 The same as those shown in Fig. 9 but for the JJA.



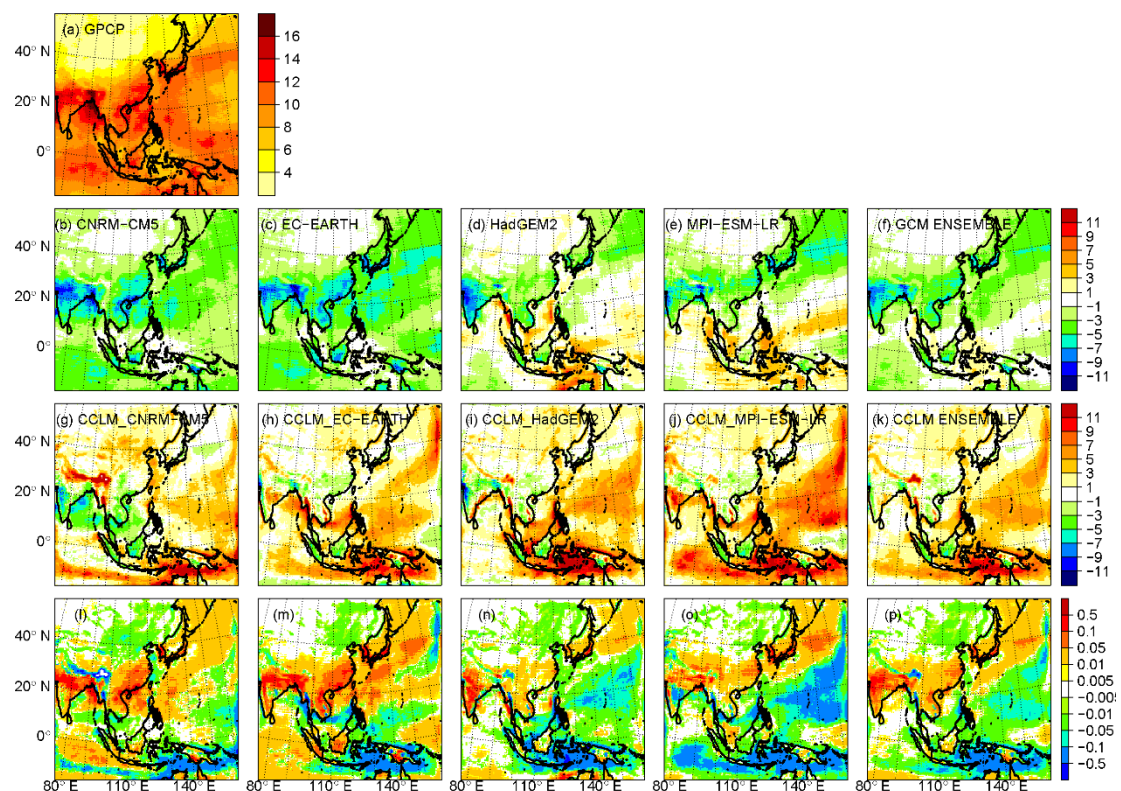
1097

1098 Fig. 11 (a) Winter (DJF) mean water vapor mixing ratio (shading, g/kg) and wind vectors
 1099 (arrows, m/s) for the ERAI reanalysis (b-e) biases of four CCLM simulations relative to
 1100 (a). (f-i) Biases in the water vapor transport (shading and arrows, $\text{ms}^{-1}\text{gkg}^{-1}$) of CCLM
 1101 simulations against ERAI reanalysis data for 1996/12 –2005/11 at 850 hPa pressure
 1102 level.



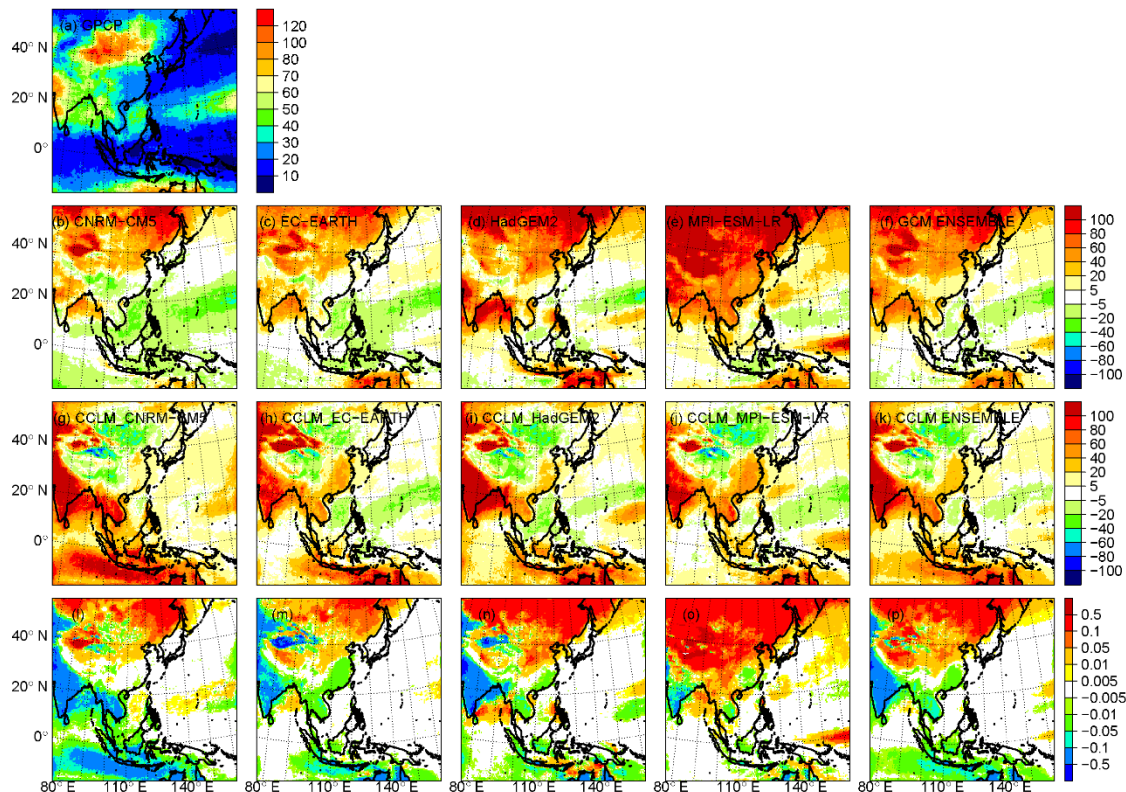
1103

1104 Fig. 12 The same as those shown in Fig. 11 but for the JJA.



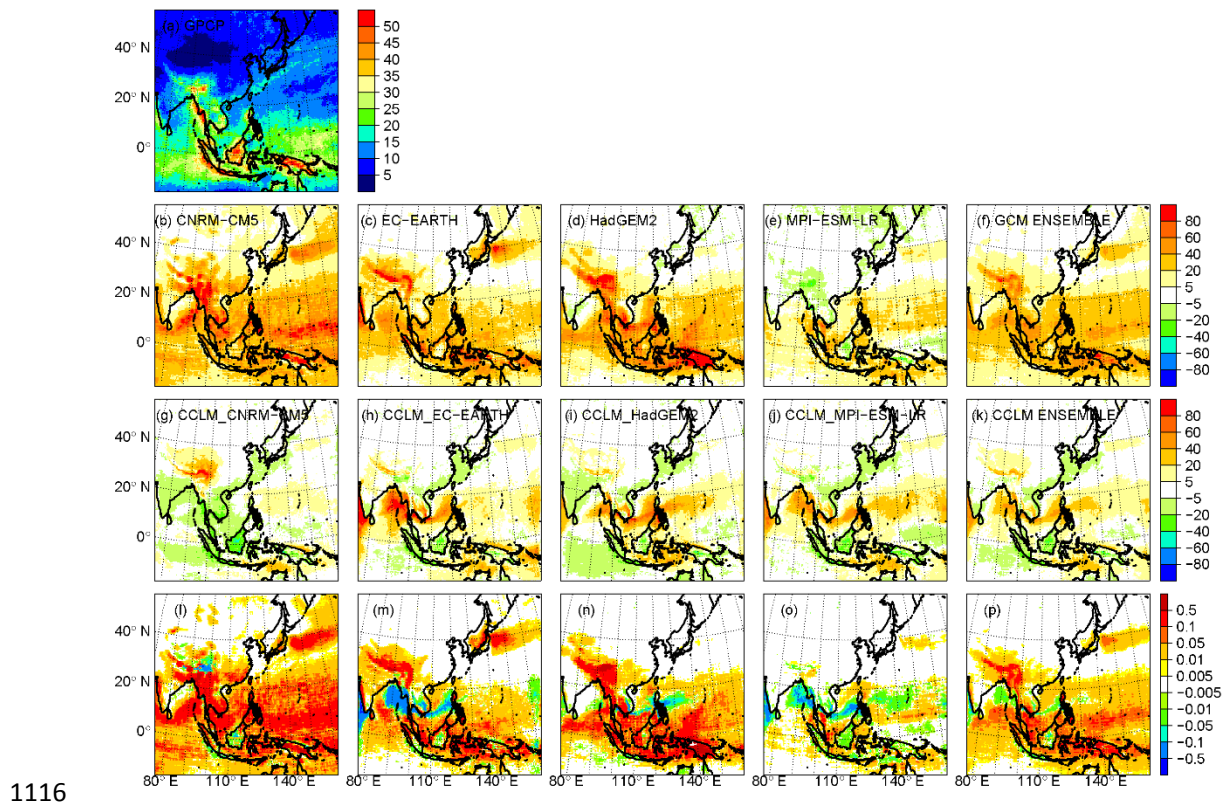
1105

1106 Fig. 13 (a) Mean precipitation amount (mm) for wet days with precipitation levels of
 1107 ≥ 1.0 mm (Simple daily intensity index, SDII index) for GPCP for 1996/12-2005/11, (b-f
 1108 and g-k) Biases (mm) of GCMs and CCLM simulations and their ensemble means
 1109 relative to the GPCP, (l-p) added value index for the SDII for each GCM-CCLM
 1110 combination.



1111
 1112 Fig. 14 The same as those shown in Fig. 13 but for the maximum number of
 1113 consecutive days with precipitation levels of < 1.0 mm (Consecutive Dry Days, CDD
 1114 index, unit: days).

1115



1116

1117 Fig. 15 The same as those shown in Fig. 13 but for the maximum number of
 1118 consecutive days with precipitation levels of ≥ 1.0 mm (consecutive wet days, CWD
 1119 index, unit: days).